Lagrangian reconstruction of snow accumulation and loss on Antarctic sea ice

Ethan C. Campbell[1], Stephen C. Riser[2], Melinda A. Webster[1]

[1] Polar Science Center, Applied Physics Laboratory, University of Washington, Seattle, Washington, USA
[2] School of Oceanography, University of Washington, Seattle, Washington, USA

Correspondence to: Ethan C. Campbell (ethancc@uw.edu)

Abstract. Snow on Antarctic sea ice strongly influences the thermodynamics and freshwater balance of the coupled sea ice–upper ocean system. Yet understanding of its temporal and spatial variations remains limited by sparse observations, large uncertainties in remote sensing retrievals, and idealized model representations. We introduce a new open-source numerical model, the University of Washington Snow on Antarctic Ice Lagrangian (WASSAIL) model, that simulates the mass and bulk density evolution of snow on sea ice in the Southern Ocean over 2003–2025. Hourly reanalysis snowfall is accumulated along Lagrangian sea ice drift trajectories determined from remotely sensed ice motion fields. The single-layer model incorporates physically and empirically informed parameterizations of key erosion and transformation processes, including surface and wind-blown snow sublimation, lead trapping, rain- and non-rain-related melt, compaction from wind and overburden pressure, and the large-scale effects of sea ice convergence and divergence. Model parameters are calibrated using snow buoy measurements from the Weddell Sea. The resulting reconstruction indicates that over one-third of annual snowfall intercepted by Antarctic sea ice is lost to the atmosphere, ocean, or to melt processes prior to complete sea ice melt, with blowing snow sublimation as the dominant sink. Comparison with satellite snow depth retrievals further suggests that widespread snow-ice formation consumes 49–60 % of the remaining snow. Overall, we infer an annual meteoric freshwater input to the Southern Ocean originating from snow on sea ice of 237 mSv, equivalent to more than half of the freshwater flux associated with circumpolar sea ice melt.

1 Introduction

In the Antarctic, the interception of snow by sea ice, its redistribution through ice transport, and subsequent melt exert a strong influence on water mass transformation and sea ice mass balance in the Southern Ocean (Abernathey et al., 2016; Haumann et al., 2016). Snow has a thermal conductivity over 6 times lower than sea ice and therefore insulates the underlying ice, reducing the rate of basal ice growth while increasing the susceptibility of sea ice to ocean heat fluxes (Semtner, 1976; Eicken et al., 1995; Massom et al., 2001). At the same time, thick snow shields ice from solar radiation and the atmosphere, helping to maintain perennial ice in areas such as the western Weddell and Bellingshausen seas (Eicken et al., 1995). Thus, snow has competing effects on the sea ice mass budget. Recent decreases in Antarctic sea ice extent (Purich and Doddridge, 2023; Wang et al., 2024a) raise questions about the ongoing role of snow in sea ice mass balance, as well as in modulating the freshwater balance of the upper ocean, its stratification, and ocean-ice heat fluxes.

Snow on Antarctic sea ice affects not only the coupled ocean-ice-snow system, but also the measurement of ice thickness itself. The depth and density of overlying snow must be known to account for its isostatic contribution when estimating ice thickness using satellite altimetry, and snow parameters are among the largest sources of uncertainty (Tilling et al., 2015). While it is known that snow on Antarctic sea ice is generally thicker than in the Arctic (Massom et al., 2001), its depth and density remain poorly constrained and a reliable climatological baseline is lacking (Webster et al., 2018). Available measurements are sparse due to the difficulty of accessing the Southern Ocean in winter. Existing measurements include visual records of snow thickness on ice floes overturned along the hull of passing ships (Worby et al., 2008), in situ measurements from snow pits, probes, and cores (e.g., Sturm et al., 1998; Arndt and Paul, 2018), and accumulation records from autonomous instruments on drifting pack ice and fast ice (e.g., Nicolaus et al., 2021; Arndt et al., 2024).

Remote sensing offers the promise of continuous circumpolar estimates of snow depth on Antarctic sea ice, albeit with different challenges. Antarctic snow depth has long been estimated using empirical algorithms applied to passive microwave radiometry (Yan et al., 2026, and references therein), but these retrievals are sensitive to weather effects, snow wetness, salinity, and grain size, and ice deformation (e.g., Kern et al., 2011; Markus et al., 2011; Rostosky et al., 2020). Satellite laser or radar altimetry, alone or combined, have also been used (e.g., Kacimi and Kwok, 2020; Fons et al., 2023), as have airborne surveys from Operation IceBridge (OIB) (e.g., Kwok and Kacimi, 2018). Overall, the utility of remote sensing estimates has been limited by several factors: uncertainties in the radar penetration depth within the snowpack (e.g., Ricker et al., 2014; Kacimi and Kwok, 2020), short coverage periods, lack of up-to-date data, necessary time averaging, and scarcity of seasonally and regionally diverse validation data sets.

Observationally constrained model reconstructions are a natural solution, but these still require validation data as well as accurate forcing and realistic process-oriented physics. The latter presents a challenge: for example, estimates of snow loss due to trapping of wind-blown snow in leads vary widely from 0 % to 50 % of all deposited snow (Eicken et al., 1994; Déry and Tremblay, 2004; Leonard and Maksym, 2011; Toyota et al., 2016; Liston et al., 2020; Clemens-Sewall et al., 2023). The importance of processes like sublimation (Fichefet and Morales Maqueda, 1999; Déry and Yau, 2002; Chung et al., 2011) and rainfall on snow (Dou et al., 2019; Boisvert et al., 2020; Stroeve et al., 2022) is also uncertain in the Antarctic. These processes are highly dependent on the variable weather conditions around Antarctica, where abrupt changes in wind, temperature, and precipitation are common (Arndt et al., 2025). Additionally, the formation of snow-ice from isostatic flooding of the snowpack by seawater – ubiquitous in the Antarctic, unlike in the Arctic (Massom et al., 2001) – cannot be constrained by model reconstructions without knowledge of sea ice thickness.

Existing model reconstructions of snow on Antarctic sea ice have either simulated the net accumulation of snow along Lagrangian drift pathways or accounted for ice motion within a fixed Eulerian frame. For Antarctica, these include a climatologically forced coupled sea ice–ocean modeling study that accounted for snow-ice formation, snow surface sublimation, and lead trapping (Fichefet and Morales Maqueda, 1999); an Eulerian simulation forced by ERA-40 reanalysis that represented snow-ice formation and the effects of ice divergence (Maksym and Markus, 2008); and the recent CPOM Antarctic Snow on Sea Ice Simulation (CASSIS), a Lagrangian model forced by ERA5 reanalysis that incorporates blowing snow loss to the ocean, katabatic transport from the Antarctic continent, and a fixed snow-ice formation fraction (Lawrence et al., 2024). In the Arctic, efforts include Lagrangian reconstructions that focused on accumulation only (Kwok and Cunningham, 2008) or approximated the effects of sublimation and divergence (Blanchard-Wrigglesworth et al., 2018); the NASA Eulerian Snow on Sea Ice Model (NESOSIM), a two-layer snow budget model with parameterizations of accumulation, compaction, lead trapping, and ice divergence (Petty et al., 2018; Cabaj et al., 2023); and SnowModel-LG, a multilayer Lagrangian snow evolution model simulating sublimation (surface and blowing snow), melt, superimposed ice, and ice dynamics (Liston et al., 2020). While each approach has provided valuable insight, many have relied on ad hoc or poorly constrained parameterizations, which may reduce confidence in some reconstructions' ability to accurately capture the temporal evolution of snow.

A more robust reconstruction methodology could illuminate the fate of snow deposited on Antarctic sea ice by identifying the factors controlling net accumulation in time and space and quantifying when, where, and how much freshwater from snowfall enters the Southern Ocean. Therefore, we develop a new model of snow evolution on Antarctic sea ice, the University of Washington Snow on Antarctic Ice Lagrangian (WASSAIL) model, which integrates snow accumulation, erosion, and transformation mechanisms (Sect. 2.3). The model is driven by reanalysis and remote sensing data and calibrated and evaluated using in situ observations from drifting snow buoys (Sect. 2.1 and 2.2). We adapt and synthesize parameterizations with firm physical or empirical bases (Sect. 2.4) and adjust their relative magnitudes to optimize the model fit to the buoy observations (Sect. 2.5). Finally, we assess calibration results (Sect. 3.1); quantify the climatological snow budget, associated freshwater fluxes, and spatial patterns (Sect. 3.2, 3.3, and 3.4); and compare our estimates to remote sensing retrievals of snow depth, enabling the inference of snow-ice formation, and discuss bulk snow density (Sect. 3.5).

2 Data and methods

2.1 Model input data

Data used as input for the WASSAIL model to simulate snow conditions from 15 February 2003 to 14 February 2025 come from a variety of remote sensing and reanalysis sources. All products were regridded to the European Centre for Medium-Range Weather Forecasts (ECMWF) ERA5 reanalysis grid, uniform in longitude and latitude (0.25° × 0.25°), using a geospatial bilinear remapping algorithm.

2.1.1 Sea ice concentration

Daily sea ice concentration (SIC) from passive microwave satellite radiometry, $f_{\mathrm{SIC,PMW}}$ (0–100 %), measured by the Advanced Microwave Scanning Radiometer for EOS (AMSR-E; 2002–2011) and AMSR2 (2012–present) sensors were obtained from the University of Bremen's ARTIST Sea Ice (ASI) product, version 5.4, on a 6.25 km polar stereographic grid (Spreen et al., 2008). AMSR-E/2 data were unavailable on 289 d during the simulation period, including the 273 d from 5 October 2011 to 3 July 2012 between the two sensors. These days of missing data were filled using SIC measured by the Special Sensor Microwave Imager (SSM/I) and Special Sensor Microwave Imager/Sounder (SSMIS) radiometers, obtained from the National Oceanic and Atmospheric Administration (NOAA) and National Snow and Ice Data Center (NSIDC) Climate Data Record (CDR) product, version 5, through 31 December 2024 and the NOAA/NSIDC Near-Real-Time (NRT) CDR product, version 3, from 1 January 2025 onwards, both provided on a coarser, 25 km grid (Meier et al., 2024a, b). Additionally, AMSR-E/2 SIC data were partially missing on 41 d, typically within narrow streaks or swatches, identified when >750 grid cells showed ≥50 % SIC differences between the AMSR and CDR products after remapping to the ERA5 grid and filling missing values with a SIC of 0 %. On these days, the CDR or NRT CDR estimates were substituted in the missing cells. Both the ASI and CDR algorithms likely underestimate SIC in thin, compact ice (Ivanova et al., 2015), with implications for accurately estimating lead fractions and constraining blowing snow loss.

2.1.2 Passive microwave snow depth

Passive microwave snow depth retrievals from AMSR-E and AMSR2 are used for model initiation each year and for validation. The NSIDC AMSR-E/2 Level 3 products on a 12.5 km polar stereographic grid are derived from an empirical algorithm developed using SSMI data in the Southern Ocean based on the spectral gradient ratio between the 18.7 and 37 GHz vertical polarization channels (Markus and Cavalieri, 1998; Cavalieri et al., 2014; Meier et al., 2018). Limitations include a technical upper retrieval limit of 0.5 m and applicability to dry snow conditions only, though values >0.5 m are still provided. These generally occur only in the western Weddell Sea at free-running model initiation (15 February of each year; see Sect. 2.3), so potential biases mainly affect this region of multiyear sea ice and the northern Weddell Sea, which receives advected ice. Validation of AMSR-E snow depths against Arctic OIB measurements showed a mean difference of 0 ± 7 cm (Brucker and

Markus, 2013), whereas comparison between a comparable AMSR2 product and OIB in the Antarctic – focusing largely on regions with multiyear ice, whose emission signal can resemble snow – found a bias of –19 cm (Shen et al., 2022).

Due to weather contamination and uncertainties in snow grain size and density, the daily fields are provided as 5 d running means; we treat them as representing the central (third) day. After regridding, snow depths from 5 d before to 5 d after Lagrangian parcel initialization were averaged to further reduce noise, such as from weather effects. During the AMSR-E/2 gap (October 2011–July 2012), the climatological value of these averages over 2003–2025 was used for model initialization instead.

2.1.3 Sea ice motion

Remotely sensed sea ice motion estimates determine the movement of Lagrangian parcels in the model (Fig. 1a). For this, we use the NSIDC Polar Pathfinder daily product, version 4.1, through 31 December 2023 and the NSIDC "Quicklook" weekly product, version 1, from 1 January 2024 onwards, both provided on a 25 km Equal-Area Scalable Earth (EASE) grid (Tschudi et al., 2019a, b, 2020). These 24 h composite estimates track ice displacement from SSM/I and SSMIS brightness temperatures using maximum cross-correlation techniques.

Schwegmann et al. (2011) evaluated the Polar Pathfinder product, version 3, against a compilation of Weddell Sea drifting sea ice buoys and found drift speeds were biased low by 34.5 % (mean $\Delta u_\mathrm{i} = -1.2$ cm s^{-1} and $\Delta v_\mathrm{i} = -1.0$ cm s^{-1}). Nonetheless, drift vector components were well-correlated with the buoys ($r \approx 0.6$), indicating good agreement in drift direction. In version 4, corrections to over-filtering of motion vectors increased Antarctic-wide drift speeds by ~1 cm s^{-1} during the SSM/I–SSMIS period from 1987 onwards (Tschudi et al., 2020) and addressed circular artifacts that had been previously identified (Szanyi et al., 2016). As version 4 largely resolves the slow bias assessed by Schwegmann et al. (2011), we do not apply the scaling factor of 1.357 calculated by Haumann et al. (2016) for the version 3 data.

Prior to remapping to the ERA5 grid, the EASE-oriented ice motion components were rotated to yield eastward and northward vectors (u_i, v_i). Weekly data for 2024–2025 were assigned to the central (fourth) day and linearly interpolated to daily resolution, and linear interpolation was also used to fill 9 missing days during 2003–2023. Grid cells with missing drift vectors but SIC >0 % – typically within two narrow bands along the ice edge and the Antarctic continent – were filled using two-dimensional nearest-neighbor interpolation based on grid cell indices (rather than geospatial distance). This approach prevents simulated Lagrangian sea ice parcels adjacent to the Antarctic continent from remaining static and accumulating excessive amounts of snow, though it allows some parcels to unrealistically originate from or transit through areas of landfast ice. A visual comparison of parcel trajectories with a mapping of Antarctic fast ice indicates this is uncommon, except near the persistent fast ice offshore of the Filchner-Ronne Ice Shelf in the Weddell Sea (Fraser et al., 2021).

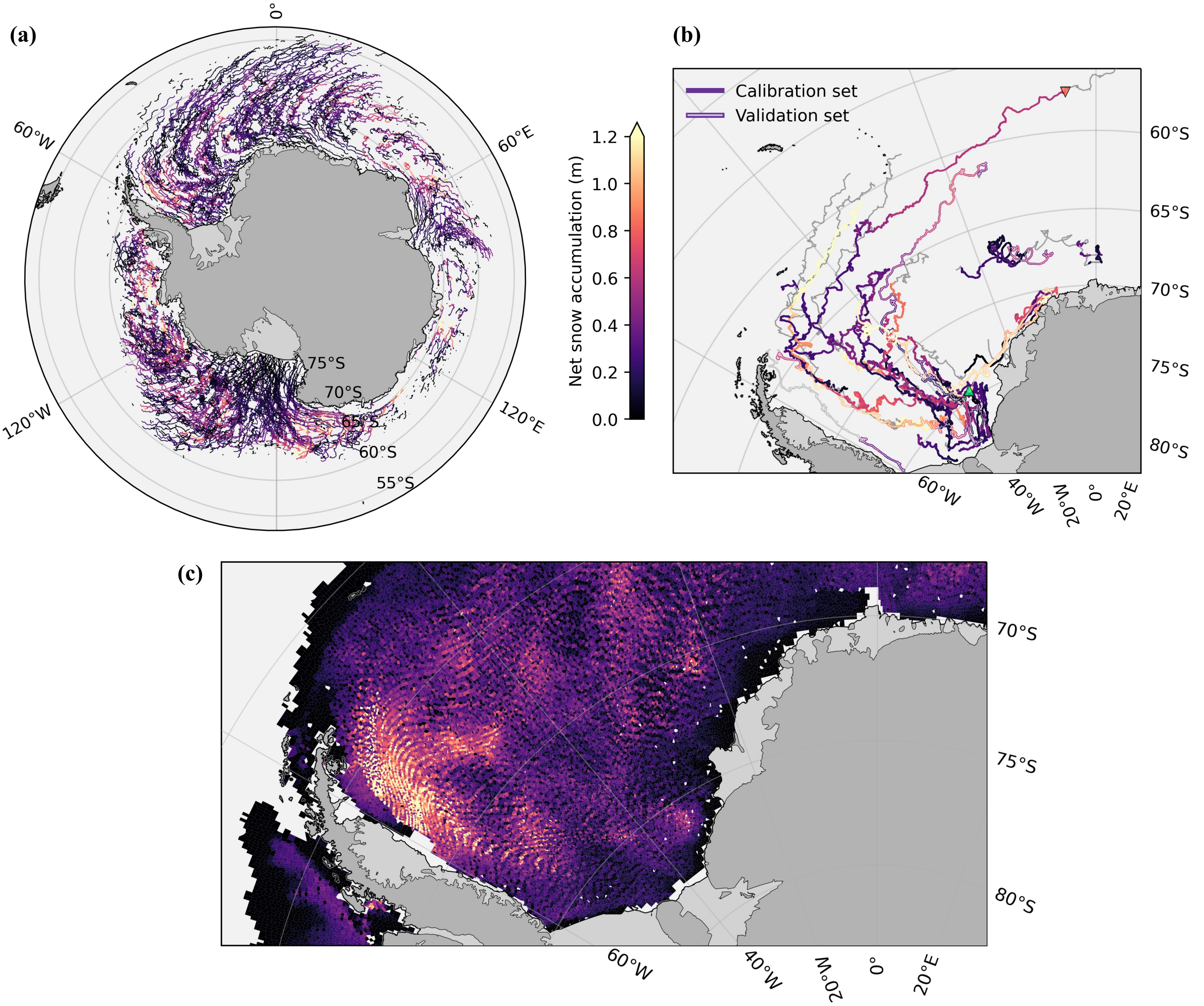

Figure 1. Simulated sea ice parcels and observed snow buoy drift trajectories. **(a)** One year of sea ice parcel advection simulated from 15 February 2021 to 14 February 2022, with parcel movement determined using remotely sensed ice motion vectors. Every 250th parcel is shown here. Lines are colored by the reconstructed net snow accumulation. **(b)** Drift trajectories of the 39 snow buoys in the Weddell Sea from 2013 to 2025, with colors indicating net snow accumulation measured by the buoys and grey lines indicating periods lacking data. Buoy assignments to the data sets used for model calibration and validation are denoted using solid and open lines, respectively. Green and red triangles mark the locations of the deployment and final valid measurement of buoy 2014S9, whose observations are examined in Fig. 5. **(c)** Example showing the computed Voronoi tessellation of simulated sea ice parcels in the Weddell Sea on 15 August 2021, with the color of each polygon indicating net snow accumulation.

2.1.4 Atmospheric reanalysis

ECMWF's ERA5 fifth-generation atmospheric reanalysis, produced using 4D-Var data assimilation, provided input to the snow model parameterizations (Hersbach et al., 2020; Copernicus Climate Change Service, 2023). Hourly 0.25° × 0.25° fields, including preliminary near real-time data from 2025, were obtained for: time-mean snowfall rate (S) and total precipitation rate (P_{tot}, kg m^{-2} s^{-1}), from which rainfall rate ($R = P_{\mathrm{tot}} - S$; expressed below in kg m^{-2} h^{-1}) was calculated; eastward and northward 10 m wind components (u_{10}, v_{10}; m s^{-1}), from which wind speed (U_{10}) was derived; 2 m air temperature (T_{a}, °C); 2 m dewpoint temperature (T_{d}, K); and surface atmospheric pressure (P_{s}, hPa).

Evaluation of ERA5 against other reanalyses shows strong consistency in the spatial patterns and interannual variability of snowfall over the Southern Ocean but a spread of ~200 mm per year in snowfall magnitude across five products (Boisvert et al., 2020). Within the ice-covered region, ERA5 snowfall exhibits a spatial distribution similar to CloudSat-derived estimates. The large uncertainty in snowfall magnitude, but not its large-scale patterns, motivates the inclusion of a scaling parameter for ERA5 snowfall in our model calibration, a practice that has been implemented in other snow modeling applications (e.g., Liston et al., 2020).

As with other atmospheric analyses, ERA5 exhibits a warm bias in estimated surface temperature over Antarctic and Arctic sea ice, likely stemming from its representation of low clouds and from treating sea ice as a constant-thickness slab without snow cover (Graham et al., 2019; Wang et al., 2019, 2024b). Nonetheless, we use near-surface air temperatures from ERA5 without correction for two reasons: biases appear small near 0 °C (Graham et al., 2019; King et al., 2022), where they would be most consequential, and are only well-quantified in the Antarctic for sea ice skin temperatures – rather than near-surface air temperatures – under clear-sky conditions (Wang et al., 2024b), which are less relevant to snow mass accumulation and loss processes.

Other key ERA5 parameters appear reasonably accurate over sea ice, with studies reporting minimal 10 m wind speed bias (<0.2 m s^{-1} at wind speeds >5 m s^{-1}) and small surface pressure biases over Weddell Sea pack ice (King et al., 2022) as well as negligible 10 m wind speed bias over Arctic sea ice (Graham et al., 2019).

2.2 Calibration, validation, and comparison data

2.2.1 Snow buoys

Snow accumulation observations from 39 snow buoys drifting on sea ice in the Weddell Sea between 2013 and 2025 (Nicolaus et al., 2017) are used to calibrate free parameters in the snow model and validate the optimized model (Fig. 1b). We exclude two snow buoys with short records (2025S142, 2025S143) and six that remained relatively stationary on landfast ice in Atka Bay, Queen Maud Land, but include six others deployed on fast ice in Atka Bay that later broke out into the Weddell Sea (2018S56, 2019S88, 2020S55, 2022S110, 2023S111, 2024S120). The snow buoys, developed by the Alfred Wegener Institute (AWI) and MetOcean Telematics, consist of a main body installed below the ice surface and a mast carrying a cross-shaped frame with four ultrasonic sensors 1.5 m above the main body, each measuring the distance to the snow surface at approximately hourly resolution with an accuracy of 1 cm (Nicolaus et al., 2021). The platform also includes a surface temperature sensor (with an accuracy of 0.5 °C), barometer, ice ablation shield, and GPS and data transmission modules. Buoy lifetimes range from ~1 month to 1–2 years. We average snow height across the four ultrasonic sensors and linearly interpolate gaps of ≤1 d. Near-real-time data from active buoys 2025S135, 2025S141, and 2025S144 were quality-controlled by removing data spikes, defined from visual inspection as any measurement ≥0.9 m. The full set of 39 buoys was randomly partitioned ~75 %–25 % into a "calibration set" of 29 buoys and a "validation set" of 10 buoys (labeled in Figs. 1b and 4).

The Lagrangian nature of snow buoy records, collected on drifting ice floes, enables a direct comparison with simulated Lagrangian parcels. Additionally, snow buoys track changes in the surface (air–snow or air–ice) interface relative to their deployment baseline, so basal snow-ice conversion following seawater infiltration will reduce actual *snow depth* (or thickness) with minimal change in the measured surface height, or *net snow accumulation* (Arndt et al., 2024). This is advantageous for model calibration, as snow-ice conversion is not represented in our model and thus buoy data provide a close analogue to reconstructed snow accumulation along the same drift trajectories, albeit as point measurements rather than grid cell averages. By contrast, ship-based snow depth observations exclude snow incorporated into basal layers of ice and are also known to be biased toward thinner, undeformed sea ice and snow due to the nature of ship navigation (Worby et al., 2008). These caveats preclude a meaningful comparison with our model, so we do not use ship-based observations from the Antarctic Sea Ice Processes and Climate (ASPeCt) archive for calibration or validation – in contrast to the approach taken with CASSIS (Lawrence et al., 2024).

2.2.2 CryoSat-2 snow depth estimates

A retrieval of snow depth on Antarctic sea ice from CryoSat-2 radar altimetry is compared with model output, alongside AMSR-E/2 snow depth estimates. The CryoSat-2 method estimates snow depth by applying waveform modeling and an optimization procedure to individual radar returns, which in theory identifies the true snow-ice interface and avoids underestimation biases that arise when a shallower scattering horizon within the snowpack (often caused by seawater wicking) is mistaken for that interface (Fons et al., 2023). The retrieved snow depths compare well with a separate product derived from CryoSat-2 and ICESat-2 (Kacimi and Kwok, 2020) and, as expected, skew higher than ship-based ASPeCt observations. The monthly estimates span July 2010–August 2021 and are provided on a 25 km polar stereographic grid; here they are averaged into a monthly climatology and remapped to the ERA5 grid as described in Sect. 2.1.

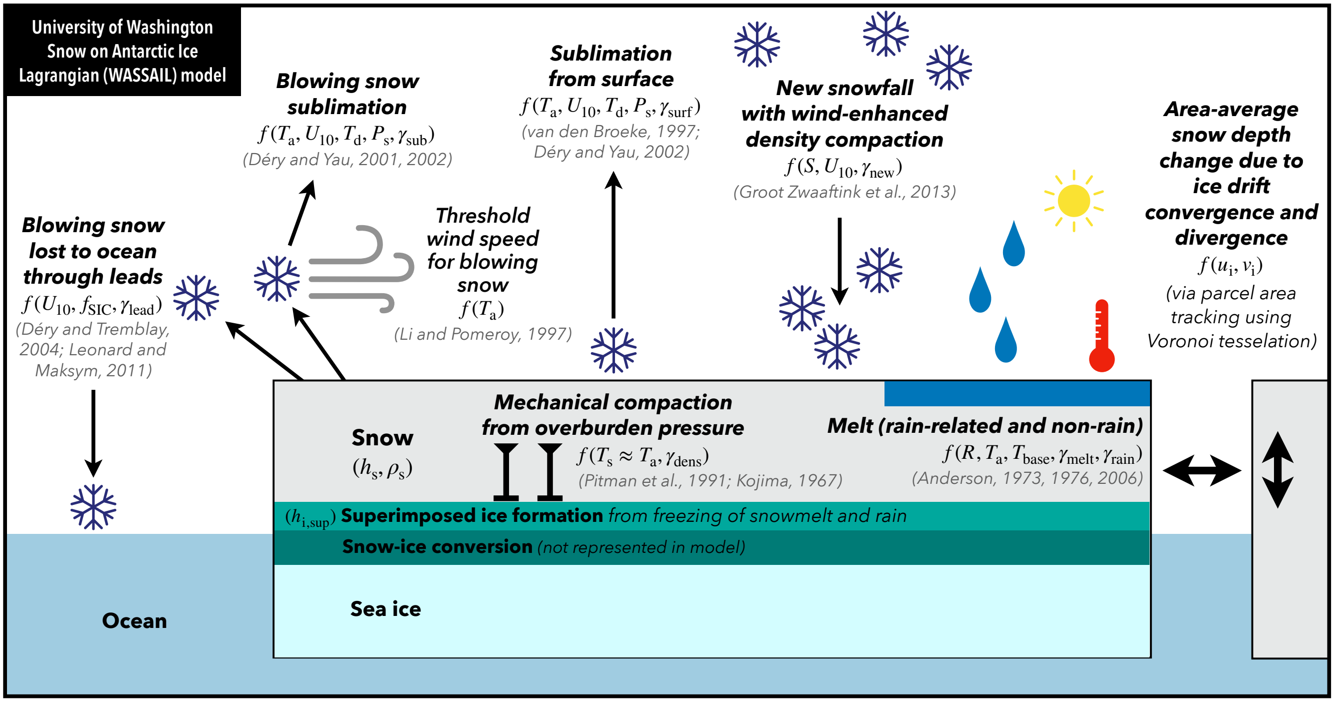

Figure 2. Summary of snow input, loss, and transformation processes represented in the University of Washington Snow on Antarctic Ice Lagrangian (WASSAIL) model. For each process, we note its primary originating source(s) and dependencies on input data and parameters (beyond snow depth and bulk density). T_s refers to the snow surface temperature.

2.3 Model overview

The single-layer WASSAIL model is intended to capture the most critical accumulation, loss, and transformation processes for reconstructing snow depth and density on Antarctic sea ice, with sufficient complexity to express key parameter dependencies (Fig. 2) while remaining computationally efficient enough for iterative calibration (Sect. 2.5). The model budget for snow accumulation on sea ice is expressed as the sum of the following terms (all in units of meters of snow per hour), which act sequentially in the order listed:

$$\frac{\partial h_s}{\partial t} = Q_{dyn} - Q_{dens} - Q_{melt} - Q_{rain} + Q_{dep} - Q_{sub} - Q_{lead} - Q_{surf}\,, \tag{1}$$

where $\frac{\partial h_s}{\partial t}$ is the net accumulation rate of snow depth; Q_{dyn} represents the net large-scale effect of sea ice dynamics, namely area-averaged snow thickening due to ice convergence and thinning due to divergence and subsequent snow-free new ice formation; Q_{dens} is mechanical compaction of the snowpack; Q_{melt} and Q_{rain} are non-rain-related and rain-related snow melt, respectively, with meltwater assumed to refreeze into a layer of superimposed ice; Q_{dep} is the rate of new snow deposition, accounting for wind-enhanced compaction of fresh snow; Q_{sub} is sublimation of wind-blown snow; Q_{lead} is loss from blowing snow trapped in leads, assumed to melt into the ocean; and Q_{surf} is sublimation from the snow surface. Free parameters are included in all budget terms except Q_{dyn}, enabling their joint adjustment to optimize the model fit to snow buoy observations (Sect. 2.5). Model parameter settings and constants are summarized in Table 1.

The model evolves four main state variables: snow depth, h_{s} (m); bulk snow density, ρ_{s} (kg m^{-3}); superimposed ice thickness, $h_{\mathrm{i,sup}}$ (m); and parcel area (km^2; see Sect. 2.4.7). In brief, ERA5 hourly reanalysis snowfall is accumulated along Lagrangian trajectories determined by Polar Pathfinder sea ice motion vectors. Changes in snow depth and bulk density due to the deposition, loss, and transformation processes in Eq. (1) are then computed using ERA5 reanalysis variables, supplemented by passive microwave SIC data (Sect. 2.4). Lastly, model output along the trajectories is binned and gridded in a volume- and mass-conserving manner, allowing analysis in an Eulerian frame of reference (Sect. 2.4.8).

The model is normally initialized with Lagrangian "parcels", each representing a large region of drifting sea ice. In calibration mode, however, each parcel corresponds to point measurements from a snow buoy, with parcel trajectories in longitude, latitude, and time prescribed by the buoy record. In free-running mode, parcels are initialized on February 15, near the climatological Antarctic sea ice extent minimum, and evolve until February 14 of the following year. Parcels are then re-initialized without memory of the prior year, preventing interannual drift from accumulated biases and enabling efficient parallelization of one-year model runs across multiple server cores. This procedure, however, limits the model's influence on snow over multiyear sea ice.

The model period (15 February 2003–14 February 2025) was chosen based on the availability of AMSR-E/2 snow depth data beginning in June 2002. In free-running simulations, sea ice parcels are initialized at every 0.25° × 0.25° grid point where SIC $\geq f_{\mathrm{SIC,0}} = 15$ %, with initial snow depth set to the ±5 d average AMSR-E/2 value (see Sect. 2.1.2). In calibration mode, parcels are instead initialized at the precise snow buoy locations using the ±5 d average AMSR-E/2 snow depth from the nearest grid cell. The snow density on pre-existing parcels is set initially at $\rho_{\mathrm{s,0}} = 320$ kg m^{-3} (Massom et al., 1997; Song et al., 2020), which is also used to normalize terms in the snow depth tendency budget (Fig. 7), and superimposed ice thickness is initialized as 0 cm. In free-running mode, parcel areas are calculated at initialization using Voronoi tessellation (Sect. 2.4.7; Fig. 1c).

The model advances using an outer loop with a daily time step that updates parcel locations, creates new parcels, and removes parcels that no longer represent sea ice. In free-running simulations, parcel longitude and latitude are updated using the azimuth and displacement derived from the previous day's Polar Pathfinder ice motion vectors. Parcels whose nearest-grid-point SIC $\leq f_{\mathrm{SIC,0}}$ are marked as having ceased to exist – that is, the ice is assumed to have completely melted into the ocean. Under this simplification, sea ice presence is treated as binary; existing snow depths are unaffected by SIC fluctuations between $f_{\mathrm{SIC,0}}$ and 1.0, though new snowfall is reduced to account for direct fluxes into leads (Sect. 2.4.2). When a parcel is removed, the model records the deposition of its snow and superimposed ice into the ocean, storing the date, the midpoint location between the

Table 1. Parameter settings and constants in the snow model.

Parameter or constant	**Value**	**Significance and origin**
Δt	1 h	Model time step for calculation of all snow depth tendency terms in Eq. (1) except for Q_{dyn}
$\rho_{\mathrm{s,0}}$	320 kg m^{-3}	Bulk snow density for model initiation and normalization of fluxes in model output (Massom et al., 1997; Song et al., 2020)
$\rho_{\mathrm{i,sup}}$	850 kg m^{-3}	Superimposed ice density (Nicolaus et al., 2003)
ρ_{i}	917 kg m^{-3}	Density of sea ice
ρ_{w}	1000 kg m^{-3}	Density of liquid water
$f_{\mathrm{SIC,0}}$	0.15	Sea ice concentration threshold for sea ice parcel existence
δ_A	±0.25	Parcel area scaling tolerance when accounting for convergent or divergent ice motion
k_n	4000 K	Baseline value of the parameter representing temperature dependence of the snow compactive viscosity (Pitman et al., 1991)
R_{thresh}	0.25 mm h^{-1}	Minimum rainfall rate for rain-on-snow melt parameterization (Anderson, 2006)
UADJ	0.15 mm mbar^{-1} (6 h)$^{-1}$	6 h mean wind function factor in the NWS SNOW-17 model rain-on-snow parameterization (Franz et al., 2008)
σ	6.12×10^{-10} mm SWE K^{-4} h^{-1}	Stefan–Boltzmann constant, expressed in terms of snow melt (Anderson, 2006)
$P_{\mathrm{s,0}}$	1012 mbar	Approximate surface atmospheric pressure
z_0, z_q	1×10^{-3} m	Aerodynamic roughness lengths for momentum and moisture over sea ice (Jordan et al., 1999)
R_{d}	287.053 J K^{-1} kg^{-1}	Dry air gas constant (Stull, 2000)
R_{v}	461.5 J kg^{-1} K^{-1}	Individual gas constant for water vapor (Rogers and Yau, 1989)
κ	0.4	von Kármán constant
T_0	273.16 K	Freezing temperature of fresh water
g	9.8 m s^{-2}	Acceleration due to gravity

previous and current day, and the released snow depth (normalized to $\rho_{\mathrm{s,0}}$) and superimposed ice thickness (using $\rho_{\mathrm{i,sup}}$ = 850 kg m^{-3}, Nicolaus et al., 2003).

New parcels, representing newly formed sea ice along the ice edge or in open-water regions within the ice pack, are introduced by first binning existing parcels onto the ERA5 grid and then instantiating new parcels at grid-cell centers where SIC ≥ $f_{\mathrm{SIC,0}}$ yet no parcels are present. In free-running mode, new parcels begin with $h_{\mathrm{s}} = h_{\mathrm{i,sup}} = 0$ cm and $\rho_{\mathrm{s}} = \rho_{\mathrm{s,0}}$; in calibration mode, they are initialized using the ±5 d mean AMSR-E/2 snow depth nearest to buoy locations. Parcel areas are then updated for all active parcels and used to rescale h_{s} and $h_{\mathrm{i,sup}}$ in a volume-conserving manner to reflect large-scale ice convergence and divergence (Sect. 2.4.7). Approximately 500,000 parcels are formed and tracked in each one-year free simulation.

An inner model loop with an hourly time step updates the snow and ice state variables using the physical parameterizations described in Sect. 2.4. In free-running simulations, reanalysis and SIC values are obtained from the grid point nearest to the parcel's linearly interpolated mid-day (12:00) position. In calibration mode, the actual hourly positions of the snow buoys are used instead.

2.4 Parameterizations of snow processes

2.4.1 Compaction from overburden pressure

Snowpack density increases – and depth decreases – over time due to mechanical compaction and fragmentation of snow grains under the overlying load of snow and air, a metamorphic process that accelerates at warmer temperatures. We adopt the parameterization for snow settling (densification due to self-loading) from Pitman et al. (1991), based on a model by Kojima (1967) calibrated to field measurements of terrestrial snow in Japan. It assumes an approximately isothermal snow layer; as an approximation, we equate snowpack temperature with the 2 m air temperature, T_a (°C). The rate of change of bulk snow density (kg m^{-3} s^{-1}) is given by:

$$\frac{\partial \rho_\mathrm{s}}{\partial t} = \frac{1}{2} h_\mathrm{s} \rho_\mathrm{s}^2 g \cdot (10^7 \text{ m s kg}^{-1}) \cdot \exp\left(14.643 - \frac{\gamma_\mathrm{dens}^{-1} k_n}{\min(T_0, T_0 + T_\mathrm{a})} - 0.02\rho_\mathrm{s}\right), \qquad (2)$$

where g is gravitational acceleration (9.8 m s^{-2}), T_0 is the freezing temperature of fresh water (273.16 K), and k_n is an empirical parameter governing the temperature dependence of snow's compactive viscosity. Validation of a land surface model that applies this formulation to a single-layer snowpack showed reasonable skill in simulating snow properties after tuning k_n (Slater et al., 1998); Kojima (1967) suggested a range of 2600–4600 K for k_n. Here we adopt an initial estimate of 4000 K, following Pitman et al. (1991), and include an inverse scaling factor γ_dens for model calibration, such that larger γ_dens produces more rapid compaction. This factor likely subsumes the influence of other snow diagenetic processes not explicitly represented (e.g., grain sintering) and may also reduce bulk compaction rates to account for depth hoar or wind slab layers that inhibit settling (Sturm et al., 2002).

After computing the change in snow density, $\Delta\rho_\mathrm{s}$, over one time step (Δt = 1 h), the corresponding change in snow depth (units of meters per hour) is calculated as:

$$Q_\mathrm{dens} = \frac{h_\mathrm{s}|_{t-1}}{\Delta t}\left(\frac{\Delta\rho_\mathrm{s}}{\rho_\mathrm{s}|_{t-1} + \Delta\rho_\mathrm{s}}\right). \qquad (3)$$

2.4.2 Wind-enhanced compaction of fresh snowfall

During blowing snow events, new and recently deposited snow grains fragment during collisions with each other or the snow surface and become more rounded through abrasion and enhanced sublimation. This promotes more efficient packing upon settling, substantially increasing the density of the surface snow layer relative to fresh snowfall (Walter et al., 2024). We adopt an empirical parameterization developed by Groot Zwaaftink et al. (2013) based on 128 measurements of surface (upper 10 cm) snow density on the Antarctic Plateau, with a modification by Keenan et al. (2021) that extends it to all wind speeds. For simplicity, this formulation is applied to all new snowfall, whose density $\rho_{\mathrm{s,new}}$ is set at:

$$\rho_{\mathrm{s,new}} = (361\ \mathrm{kg\ m^{-3}}) \cdot \log_{10}\left(U_{10,100\mathrm{h}}\right) + (33\ \mathrm{kg\ m^{-3}})\ \text{when}\ U_{10,100\mathrm{h}} > 1\ \mathrm{m\ s^{-1}}\,, \tag{4}$$

$$\rho_{\mathrm{s,new}} = 33\ \mathrm{kg\ m^{-3}}\ \text{when}\ U_{10,100\mathrm{h}} \leq 1\ \mathrm{m\ s^{-1}}. \tag{5}$$

Similar to Groot Zwaaftink et al. (2013), we use the 100 h forward-looking (left-edge) rolling mean 10 m wind speed, $U_{10,100\mathrm{h}}$ (m s^{-1}), to reflect the timescale over which wind packing occurs following a snowfall event, before a new snow layer becomes strongly bonded by sintering and wind crust formation. For example, an equation developed by Box et al. (2004) to parameterize these effects based on the force required to disaggregate bonds in snow particles of a certain age (their Eq. 5) suggests that only about one-third of a fresh snow layer remains available for aeolian transport 100 h after deposition. For computational efficiency, the model implementation of $U_{10,100\mathrm{h}}$ relies on winds averaged at the snowfall location, implicitly treating drifting sea ice as stationary over the 100 h averaging period.

To obtain the change in snow depth from new snowfall over Δt = 1 h (Q_{dep}, m h^{-1}), we apply a scaling factor γ_{new} to calibrate the ERA5 reanalysis snowfall rate S (kg m^{-2} s^{-1}), whose magnitude may be biased (see Sect. 2.1.4). In free-running simulations, snowfall is further scaled by ice concentration, $f_{\mathrm{SIC,PMW}}$:

$$Q_{\mathrm{dep}} = f_{\mathrm{SIC,PMW}} \cdot \frac{\gamma_{\mathrm{new}}\, S}{\rho_{\mathrm{s,new}}} \cdot \frac{(3600\ \mathrm{s})}{\Delta t}\,. \tag{6}$$

The remaining fraction, $f_{\mathrm{OW}} = 1 - f_{\mathrm{SIC,PMW}}$, represents a direct flux to the ocean and is not considered in this study. The bulk snow density is then updated as a weighted average of the pre-existing and freshly deposited snow.

2.4.3 Non-rain and rain-related snow melt

We implement two snow-melt parameterizations: one for melt driven by changes in snowpack net energy balance associated with radiative fluxes and warm air when rainfall is absent or negligible (hereafter “non-rain” conditions), and one for melt during rain-on-snow (ROS) events. Because our model does not explicitly resolve snow thermodynamics, we adopt simple formulations from the National Weather Service (NWS) SNOW-17 operational model (Anderson, 1973, 1976, 2006), which has been used for decades in snowmelt and streamflow forecasting. Although developed for land, these functional forms capture fundamental dependencies on air temperature and rainfall rate; we add three free parameters for calibration to Antarctic sea ice conditions. Melt is permitted only when some portion of the snowpack has warmed to the freezing point, which both parameterizations assume has occurred; we rely on the tuning parameters to compensate if melt is otherwise predicted too frequently. The original ROS formulation further assumes minimal solar radiation due to overcast conditions, dewpoint and rain temperature equal to the 2 m air temperature T_{a}, and high relative humidity (~90 %).

Both snowmelt and rainfall liquid water mass are conserved in the model, assumed to percolate downward before refreezing within a new or existing superimposed ice layer with density $\rho_{\mathrm{i,sup}}$ = 850 kg m^{-3} (Nicolaus et al., 2003). Superimposed ice has been observed at the base of the snowpack on Antarctic sea ice (e.g., Arndt et al., 2021), although buried surface crusts can also form internal ice layers that intercept percolating meltwater (Massom et al., 2001). Our single-layer model is agnostic to the formation depth of these layers, and their combined thickness, $h_{\mathrm{i,sup}}$, is tracked as superimposed ice.

Non-rain melt is approximated using a "degree-day" approach and is active during hourly periods with no rain or only light rainfall ($R < R_{\mathrm{thresh}}$, where R_{thresh} = 0.25 mm h^{-1} = 0.25 kg m^{-2} h^{-1}, per Anderson, 2006). Q_{melt} (m snow h^{-1}) is computed as the smaller of the predicted melt rate or the available snow depth divided by the time step:

$$Q_{\mathrm{melt}} = \min\left(\frac{h_{\mathrm{s}}}{\Delta t}, \frac{\rho_{\mathrm{w}}}{10^3 \rho_{\mathrm{s}}} \cdot \gamma_{\mathrm{melt}}\big(\max(0\ {}^{\circ}\mathrm{C}, T_{\mathrm{a}} - T_{\mathrm{base}}) + \gamma_{\mathrm{rain}} \cdot M_{\mathrm{r,direct}}\big)\right), \tag{7}$$

where ρ_{w} is the density of liquid water (1000 kg m^{-3}) and γ_{melt} is an empirical 6 h "melt factor" relating melt rate to air temperature for a specific region. For reference, Girotto et al. (2024) offer a range of 1–2 mm snow water equivalent (SWE) °C^{-1} (6 h)$^{-1}$ for maximum summer melt in an alpine setting; we treat γ_{melt} as a tunable parameter. T_{base} is the threshold air temperature above which snow melt tends to occur ("MBASE" in SNOW-17), typically near 0 °C (Anderson, 1973), and is also treated as tunable.

γ_{rain} is the tunable scaling parameter for ROS melt. $M_{\mathrm{r,direct}}$ (mm SWE h^{-1}) in both Eqs. (7) and (9) represents melt from energy released directly within the snowpack by rainfall R (kg m^{-2} h^{-1}), including trace amounts:

$$M_{\mathrm{r,direct}} = \left(12.5\ {}^{\circ}\mathrm{C}^{-1}\right) \cdot \max(T_{\mathrm{a}}, 0\ {}^{\circ}\mathrm{C}) \cdot \frac{R}{\rho_{\mathrm{w}}}. \tag{8}$$

ROS melt applies during hourly periods of significant rainfall ($R \geq R_{\mathrm{thresh}}$), with melt rate Q_{rain} (m snow h^{-1}) given as the sum of three terms, including $M_{\mathrm{r,direct}}$:

$$Q_{\mathrm{rain}} = \frac{\rho_{\mathrm{w}}}{10^3 \rho_{\mathrm{s}}} \cdot \gamma_{\mathrm{rain}} \cdot \left(M_{\mathrm{r,direct}} + M_{\mathrm{r,rad}} + M_{\mathrm{r,turb}}\right). \tag{9}$$

The second term, $M_{\mathrm{r,rad}}$ (mm SWE h^{-1}), represents melt from net radiative transfer under the meteorological conditions typical of rainfall, notably enhanced downward longwave radiation:

$$M_{\mathrm{r,rad}} = \max\left(\begin{matrix} 0\ \mathrm{mm\ SWE\ h^{-1}}, \\ \sigma \cdot \left[(T_{\mathrm{a}} + T_0)^4 - T_0^4\right] \end{matrix}\right), \tag{10}$$

where σ is the Stefan–Boltzmann constant, expressed as snow melt (6.12×10^{-10} mm SWE K^{-4} h^{-1}).

The third term, $M_{\mathrm{r,turb}}$ (mm SWE h^{-1}), represents melt due to turbulent latent and sensible heat exchange during rainfall events:

$$M_{\mathrm{r,turb}} = \max\begin{pmatrix} 0 \text{ mm SWE h}^{-1}, \\ 8.5 \cdot \mathrm{UADJ} \cdot \left[\left(0.00057\ {}^{\circ}\mathrm{C}^{-1}\right)P_{\mathrm{s},0}T_{\mathrm{a}} + (0.9e_{\mathrm{s}} - [6.11 \text{ mbar}])\right] \end{pmatrix}, \tag{11}$$

in which UADJ is the empirical mean 6 h wind function factor during ROS periods in SNOW-17 (0.15 mm SWE mbar^{-1} [6 h]$^{-1}$; Franz et al., 2008), $P_{\mathrm{s},0}$ is a representative surface pressure (1012 mbar), and e_{s} (mbar) is the saturation vapor pressure over water at T_{a}, computed using an empirical formula from Rogers and Yau (1989):

$$e_{\mathrm{s}} = 6.112 \exp\left(\frac{17.67\ T_{\mathrm{a}}}{T_{\mathrm{a}} + 243.5}\right). \tag{12}$$

Processes related to liquid water retention in the snowpack are not explicitly represented, as rainfall and snowmelt are assumed to freeze rapidly; their cumulative effects may instead be incorporated through the tuning parameters. Relevant processes include melt metamorphism, enhanced destructive (equi-temperature) metamorphism, and reduced compactive viscosity in the presence of liquid water (e.g., Anderson, 1976; Yamazaki et al., 1993; Abolafia-Rosenzweig et al., 2024). Rain-driven metamorphism may also increase bulk snow density (Stroeve et al., 2022), but this parameterization does not resolve such density changes.

2.4.4 Snow surface sublimation

Static-surface sublimation or deposition may occur as continuous exchange between the air and the snow surface (or sea ice surface, if bare of snow). Similar to the reanalysis-based reconstruction of Déry and Yau (2002), we assume that the shallow near-surface air layer quickly becomes saturated, so surface sublimation is minimal during blowing snow events. We therefore consider surface sublimation to be conditional on 10 m wind speed, U_{10} (m s^{-1}), remaining below the threshold at which dry snow transport by saltation begins. This threshold depends on cohesion and frictional forces between snow particles and during collisions, which vary with ambient temperature. We set the threshold 10 m wind speed for snow transport, U_{t} (m s^{-1}), using the temperature-dependent formula of Li and Pomeroy (1997), with a = 9.43 m s^{-1}, b = 0.18 m °C^{-1} s^{-1}, and c = 0.0033 m °C^{-2} s^{-1}:

$$U_{\mathrm{t}} = a + bT_{\mathrm{a}} + cT_{\mathrm{a}}^2. \tag{13}$$

Field measurements of blowing snow onset on Arctic and Antarctic sea ice support this empirical relationship (Ranjithkumar et al., 2025). Following van den Broeke (1997) and Déry and Yau (2002), the supply-limited surface sublimation, Q_{surf} (m snow h^{-1}; positive for net sublimation and negative for net deposition), is calculated as:

$$Q_{\mathrm{surf}} = \max\left(\frac{h_{\mathrm{s}}}{\Delta t}, -\gamma_{\mathrm{surf}}\,\rho_{\mathrm{a}}\,u^{*}q^{*} \cdot \frac{(3600 \text{ s})}{\rho_{\mathrm{s}} \cdot \Delta t}\right) \text{ when } U_{10} < U_{\mathrm{t}}, \tag{14}$$

$$Q_{\mathrm{surf}} = 0 \text{ m h}^{-1} \text{ when } U_{10} \geq U_{\mathrm{t}}. \tag{15}$$

In Eq. (14), γ_{surf} is a tunable scaling factor and ρ_{a} is air density (kg m^{-3}), computed following Stull (2000) as:

$$\rho_{\mathrm{a}} = \frac{100P_{\mathrm{s}}}{R_{\mathrm{d}}(T_{\mathrm{a}} + T_0) \cdot (1 + 0.61q_{\mathrm{v}})} , \tag{16}$$

where P_{s} is surface pressure from ERA5 (hPa) and R_{d} is the dry-air gas constant (287.053 J K^{-1} kg^{-1}). q_{v} is specific humidity (kg kg^{-1}), computed using the 2 m dewpoint temperature from ERA5 (T_{d}; in Kelvin scale) using a form of the Magnus–Tetens equation from Kong and Yau (1997):

$$q_{\mathrm{v}} = \frac{(3.8\ \mathrm{hPa})}{P_{\mathrm{s}}} \exp\left(\frac{17.27(T_{\mathrm{d}} - T_0)}{T_{\mathrm{d}} - (35.86\ \mathrm{K})}\right) . \tag{17}$$

The remaining factors are friction velocity, u^* (m s^{-1}), a measure of shear-driven turbulence, and the humidity scale, q^* (kg kg^{-1}), the scale of turbulent moisture fluctuations. Following Garratt (1992), they are defined as:

$$u^* = \frac{\kappa U_{10}}{\ln\left(\frac{[10\ \mathrm{m}] + z_0}{z_0}\right)} , \tag{18}$$

$$q^* = \frac{\kappa q_{\mathrm{i,sat}}(\mathrm{RH_i} - 1)}{\ln\left(\frac{[10\ \mathrm{m}] + z_q}{z_q}\right)} . \tag{19}$$

In these formulae, κ is the von Kármán constant (0.4) and z_0 and z_q (m) are aerodynamic roughness lengths for momentum and moisture, respectively, which we take to be equal, $z_0 = z_q$. We adopt $z_0 = 1 \times 10^{-3}$ m, a typical sea-ice value (Jordan et al., 1999) that lies between values of 5×10^{-4} m (Andreas et al., 2010) and 4.1×10^{-3} m (Weiss et al., 2011) obtained for Antarctic sea ice using different techniques. $\mathrm{RH_i}$ is relative humidity with respect to ice at 2 m:

$$\mathrm{RH_i} = \frac{q_{\mathrm{v}}}{q_{\mathrm{i,sat}}} , \tag{20}$$

where $q_{\mathrm{i,sat}}$ is the saturation mixing ratio over ice (kg kg^{-1}) from Kong and Yau (1997), noting that T_{a} is in degrees Celsius, unlike T_{d} in Eq. (17):

$$q_{\mathrm{i,sat}} = \frac{(3.8\ \mathrm{hPa})}{P_{\mathrm{s}}} \exp\left(\frac{21.87\ T_{\mathrm{a}}}{T_{\mathrm{a}} + T_0 - (7.66\ \mathrm{K})}\right) . \tag{21}$$

In saturated conditions ($\mathrm{RH_i} > 1.0$), q^* becomes positive and net deposition, rather than sublimation, occurs.

2.4.5 Blowing snow sublimation

Blowing snow occurs when wind entrains loose snow particles from sea ice. While in suspension, snow grains can sublimate if the atmospheric boundary layer is subsaturated. We consider the following parameterization to be a maximum potential sublimation rate, $Q_{\mathrm{sub,max}}$ (m h^{-1}), neglecting snow supply, which is addressed below using the partitioning with $Q_{\mathrm{lead,max}}$ in Eq. (31). $Q_{\mathrm{sub,max}}$ depends on wind speed, temperature, and humidity and was derived by Déry and Yau (2001) using a double-moment numerical model of blowing snow, yielding estimates that correlated well (r^2 = 0.95) with sublimation observations from a Canadian Arctic tundra site. Blowing snow sublimation is permitted only when $U_{10} \geq U_{\mathrm{t}}$, as specified in Eq. (13); $T_{\mathrm{a}} <$ 0 °C; and air is subsaturated with respect to ice. We include a unit conversion factor, k (1.1574×10^{-5} d s^{-1}), and a tunable scaling factor, γ_{sub}:

$$Q_{\mathrm{sub,max}} = \gamma_{\mathrm{sub}}\, k\, Q'_{\mathrm{sub}} \cdot \frac{(3600\ \mathrm{s})}{\rho_{\mathrm{s}} \cdot \Delta t} \quad \text{when } T_{\mathrm{a}} < 0\ ^{\circ}\mathrm{C},\ U_{10} \geq U_{\mathrm{t}}, \mathrm{RH_i} \leq 1.0\,, \tag{22}$$

$$Q_{\mathrm{sub,max}} = 0\ \mathrm{m\ h^{-1}} \quad \text{when } T_{\mathrm{a}} \geq 0\ ^{\circ}\mathrm{C},\ U_{10} < U_{\mathrm{t}}, \text{or } \mathrm{RH_i} > 1.0\,. \tag{23}$$

The expression $Q_{\mathrm{sub}}{}'$ is defined as:

$$Q'_{\mathrm{sub}} = \begin{pmatrix} a_0 + a_1\xi + a_2\xi^2 + a_3\xi^3 + a_4U_{10} + a_5\xi U_{10} \\ + a_6\xi^2 U_{10} + a_7U_{10}^2 + a_8\xi U_{10}^2 + a_9U_{10}^3 \end{pmatrix} \mathrm{kg\ m^{-2}\ d^{-1}}\,, \tag{24}$$

where dimensionless coefficients a_0–a_9 are listed in Table A1 and ξ (m^2 s^{-1}) is a thermodynamic term in which ρ_{i} is sea ice density (917 kg m^{-3}):

$$\xi = \frac{-1 \times 10^{12} \cdot (\mathrm{RH_i} - 1)}{2\rho_{\mathrm{i}}(F_k + F_d)}\,. \tag{25}$$

F_k and F_d (m s kg^{-1}) represent the temperature-dependent conductivity and diffusion terms associated with snow sublimation. Following Rogers and Yau (1989; Eq. 7.17):

$$F_k = \left(\frac{10^3 \cdot L}{R_{\mathrm{v}}(T_{\mathrm{a}} + T_0)} - 1\right)\frac{10^3 \cdot L}{KT_{\mathrm{a}}}\,, \tag{26}$$

$$F_d = \frac{R_{\mathrm{v}}(T_{\mathrm{a}} + T_0)}{10^2 \cdot De_{\mathrm{s}}}\,. \tag{27}$$

In these expressions, R_{v} is the individual gas constant for water vapor (461.5 J kg^{-1} K^{-1}), e_{s} is saturation vapor pressure over water (mbar; Eq. 12), L is latent heat of condensation (J g^{-1}), K is the air thermal conductivity (J m^{-1} s^{-1} K^{-1}), and D is the water vapor diffusivity in air (m^2 s^{-1}). The latter three parameters – L, K, and D – are tabulated in Table A2 as functions of T_{a}, assuming a surface pressure of 1000 hPa for K and D. We fit third-order polynomials to interpolate between the tabulated temperatures.

This representation relies on γ_{sub} to account for the reduced lofting of older snow relative to fresh snow. Newly deposited layers rapidly "lock up", or become strongly bonded, through sintering, wind crust formation, seawater and brine wicking (capillary suction), and occasional rain penetration and refreezing (Sect. 2.4.2; Sturm et al., 1998; Arndt et al., 2025), inhibiting saltation and suspension. Explicitly representing lock-up would require tracking the age distribution of snowfall events and snowpack stratigraphic evolution; we leave this to future versions of the WASSAIL model. γ_{sub} also subsumes other physical processes that limit available snow for aeolian transport, such as preferential accumulation along ridges or other features that aerodynamically shelter snow. Field observations off East Antarctica indicate such sheltering can substantially reduce snow loss to leads in areas of rough, deformed ice (Toyota et al., 2016), and observations in the Bellingshausen Sea suggest that blowing snow may occur only about half the time that wind speeds exceed the Li and Pomeroy (1997) threshold U_{t} (Leonard and Maksym, 2011).

2.4.6 Transport into leads

Blowing snow may drive significant snow loss into leads ("lead trapping") and preferential redistribution along microrelief and ridges in regions of deformed ice, with both processes governed by the balance of snow suspension, saltation, and gravitational settling and by lead geometry and surface roughness. While redistribution is otherwise neglected given the WASSAIL model's large-scale, area-averaged snow mass budget, lead trapping is a potentially important snow sink as well as an immediate freshwater flux to the ocean if deposited snow melts in leads rather than refreezing as slush (see discussion in Sect. 3.4). For simplicity, we assume trapped snow melts immediately in the ocean.

A boundary-layer blowing snow model by Déry and Tremblay (2004) indicates that lead trapping efficiency depends primarily on along-fetch lead size and spacing, wind speed, and friction velocity, and that leads can collect ~60–100 % of blowing snow under a range of conditions. We adopt that study's parameterization of the maximum potential deposition of blowing snow into the ocean through leads (units of meters per hour) during periods of active wind transport ($U_{10} \geq U_{\mathrm{t}}$; Sect. 2.4.4):

$$Q_{\mathrm{lead,max}} = \gamma_{\mathrm{lead}}\, f_{\mathrm{OW}}\, Q'_{\mathrm{lead}} \cdot \frac{(0.0417\ \mathrm{d})}{\rho_{\mathrm{s}} \cdot \Delta t} \text{ when } U_{10} \geq U_{\mathrm{t}}\,, \tag{28}$$

$$Q_{\mathrm{lead,max}} = 0\ \mathrm{m\ h^{-1}} \text{ when } U_{10} < U_{\mathrm{t}}\,. \tag{29}$$

The local open-water fraction ($f_{\mathrm{OW}} = 1 - f_{\mathrm{SIC,PMW}}$) is obtained from daily AMSR-E/2 SIC at 6.25 km resolution (Sect. 2.1.1). Déry and Tremblay (2004) find that snow loss to leads varies by over 2 orders of magnitude across lead spacings of 0.1–10 km, but surprisingly little across lead widths, implying that the number density of leads is more influential than open-water fraction. Nonetheless, we use f_{OW} as an imperfect proxy for lead frequency or density, since current products for the Southern

Ocean are limited to winter (Petty et al., 2021; Dubey et al., 2025). The tunable scaling factor γ_{lead} is intended to account for the uncertain relationship between f_{OW} and lead density/width, varying lead orientations relative to winds, limits on available snow for aeolian transport (e.g., diagenetic processes, aerodynamic shielding), and uncertainty in the trapping efficiency and parameterization of Q'_{lead} below.

A functional form is adopted for the relationship between Q'_{lead}, the snow mass flux into leads (mm SWE d^{-1} ≡ kg m^{-2} d^{-1}), and U_{10} based on the simulations of Déry and Tremblay (2004; their Table 1, reproduced below as Table A3), assuming a 1 km lead spacing, following Eicken et al. (1994). We fit a third-order polynomial to the Q'_{lead} tabulation, specified in 5 m s^{-1} wind speed increments, after adding a point at Q'_{lead} = 0 mm SWE d^{-1} for U_{10} = 0 m s^{-1}:

$$Q'_{\text{lead}} = (-0.0357 + 3.9083 \cdot U_{10} - 0.4026 \cdot U_{10}^2 + 0.0141 \cdot U_{10}^3) \text{ mm SWE d}^{-1} . \tag{30}$$

Thus, lead trapping increases dramatically at higher wind speeds as snow mass is transported over leads more efficiently.

If the sum of the potential blowing snow sublimation ($Q_{\text{sub,max}}$) and lead trapping ($Q_{\text{lead,max}}$) exceeds the current snow depth (h_s), these maximum values are used as weights to partition the available blowing snow:

$$Q_{\text{sub}} = \min\left(Q_{\text{sub,max}}, \left[\frac{Q_{\text{sub,max}}}{Q_{\text{sub,max}} + Q_{\text{lead,max}}} \cdot \frac{h_{\text{s}}}{\Delta t}\right]\right) , \tag{31}$$

$$Q_{\text{lead}} = \min\left(Q_{\text{lead,max}}, \left[\frac{Q_{\text{lead,max}}}{Q_{\text{sub,max}} + Q_{\text{lead,max}}} \cdot \frac{h_{\text{s}}}{\Delta t}\right]\right) . \tag{32}$$

2.4.7 Effects of ice dynamics

As simulated Lagrangian sea ice parcels are advected (Sect. 2.3), they experience convergent and divergent motion. Assuming ice volume conservation, convergence produces area-averaged ice thickening, while divergence creates open-water areas where new ice can form, often rapidly (von Albedyll et al., 2021). We adopt an analogous volume-conserving treatment for snow depth, with dynamical thickening due to ridging and rafting under ice convergence and area-averaged thinning where divergence produces new, snow-free ice. Superimposed ice thickness is treated similarly. In reality, some snow may be lost to the ocean as it becomes submerged during ridging, but this loss is uncertain and neglected here. Existing approaches either require complex ice-deformation representations (e.g., Roberts et al., 2019) or assume an arbitrary fractional loss of snow (e.g., 50 %; Hunke et al., 2015).

We enforce snow and superimposed-ice volume conservation during ice convergence and divergence using Voronoi tessellation, a technique that geometrically subdivides a space into the polygonal regions closest to each of a set of points – in this case, sea ice parcel centroids (Fig. 1c). At each daily time step (Sect. 2.3), contiguous sea ice regions with $f_{\text{SIC,PMW}} > 0$ % are identified and a Voronoi partitioning is computed using the SciPy library (*Voronoi* function in the *spatial* subpackage;

Virtanen et al., 2020). Polygons are clipped to sea ice boundaries and projected to an EASE grid, and the area A (km^2) for each parcel's polygon is calculated. The resulting changes in snow depth h_s (and similarly $h_\mathrm{i,sup}$) from day $t-1$ to day t are, in meters of snow per hour:

$$Q_\mathrm{dyn} = \left(\frac{A|_{t-1}}{A|_t} - 1\right) \cdot \frac{h_\mathrm{s}|_t}{\Delta t} \quad \text{when } (1-\delta_A) \leq \frac{A|_{t-1}}{A|_t} \leq (1+\delta_A)\,, \tag{33}$$

$$Q_\mathrm{dyn} = 0 \text{ m h}^{-1} \quad \text{when } \frac{A|_{t-1}}{A|_t} < (1-\delta_A) \text{ or } \frac{A|_{t-1}}{A|_t} > (1+\delta_A)\,, \tag{34}$$

where δ_A is 0.25, imposing a ±25 % tolerance on daily area scaling. Instances exceeding this tolerance are uncommon and occur mainly due to truncation or expansion of Voronoi polygons along the ice edge. Although the daily area scaling factor $\left({}^{A|_{t-1}}/{}_{A|_t}\right)$ is not strictly physically meaningful for an individual parcel, whose polygonal boundaries depend on the relative position of parcel centroids, the scaling factors capture the effects of convergence and divergence upon averaging Q_dyn over time or space, reducing noise. Q_dyn may nonetheless underestimate divergence, since strongly divergent conditions can lead to a 0.25° × 0.25° grid cell becoming devoid of parcels and a new parcel being instantiated, explicitly simulating new ice formation (Sect. 2.3).

2.4.8 Conversion from Lagrangian to Eulerian frame

Tracking A enables volume (or mass) conservation when mapping the extrinsic properties h_s and $h_\mathrm{i,sup}$, snow depth tendency terms $Q_{\{\cdot\}}$, and ice–ocean fluxes of snow and superimposed ice from the Lagrangian parcel frame of reference onto a regular (Eulerian) grid. This regridding is performed after each model run for all variables recorded along parcel trajectories, including bulk snow density ρ_s. Daily values are aggregated using two-dimensional, area-weighted binning of all parcels whose centroids fall within a given ERA5 grid cell, coarsened by a factor of 3 to 0.75° × 0.75° to reduce noise, particularly in Q_dyn. For extrinsic properties and snow-depth fluxes – but not ρ_s, an intrinsic property – parcel values are additionally scaled by $\left({}^{\Sigma A}/{}_{A_{0.75°}}\right)$, where ΣA is the total parcel area within the coarsened grid cell and $A_{0.75°}$ is the latitude-dependent cell area.

2.5 Model calibration procedure

The parameterizations in Sect. 2.4 include eight tuning parameters (Table 2) that incorporate the effects of unmodeled processes and compensate for biases in input data and the parameterizations themselves. We developed an iterative procedure to adjust these parameters, optimizing model fit to observations of snow accumulation from the randomly selected calibration set of 29 snow buoys drifting in the Weddell Sea during 2013–2025 (Fig. 1b; Sect. 2.2.1), with the remaining 10 buoys reserved for model validation. The buoy-covered regions exhibit substantial spatial and interannual variability in snow-on-sea-ice

Table 2. Free parameters in the model. Listed for each tuning parameter are the introducing section, the initial value and standard deviation used to generate candidate values for the optimization procedure, the optimized value after rung 12 of the tuning ladder, and a description.

Parameter	**Section**	**Initial value**	**Initial standard deviation**	**Final value (rung 12)**	**Significance**
γ_{dens}	2.4.1	1.0	0.1	1.09	Inverse scaling factor for k_n, the compactive viscosity of snow, modifying the rate of mechanical compaction due to overburden pressure
γ_{new}	2.4.2	1.0	0.25	1.32	Scaling factor for Q_{dep}, the rate of new snowfall deposition
T_{base}	2.4.3	0.0 °C	1.0 °C	0.16 °C	Threshold air temperature in Q_{melt} above which non-rain snow melt tends to occur (~0.0 °C; Anderson, 1973)
γ_{melt}	2.4.3	1.5 mm °C^{-1} (6 h)$^{-1}$	0.5 mm °C^{-1} (6 h)$^{-1}$	2.52 mm °C^{-1} (6 h)$^{-1}$	6 h melt factor in Q_{melt} relating non-rain snow melt rate to air temperature (~1–2 mm °C^{-1} [6 h]$^{-1}$; Girotto et al., 2024)
γ_{rain}	2.4.3	1.0	1.0	1.14	Scaling factor for Q_{rain}, the snow melt rate due to significant rainfall events
γ_{surf}	2.4.4	1.0	1.0	2.04	Scaling factor for Q_{surf}, the rate of snow surface sublimation
γ_{sub}	2.4.5	1.0	1.0	1.04	Scaling factor for $Q_{\mathrm{sub,max}}$, the maximum (non-supply-limited) rate of blowing snow sublimation
γ_{lead}	2.4.6	1.0	1.0	0.35	Scaling factor for $Q_{\mathrm{lead,max}}$, the maximum (non-supply-limited) rate of lead trapping of blowing snow

properties and diverse meteorological conditions (Massom et al., 1997; Markus and Cavalieri, 2006; Arndt and Paul, 2018), albeit with lower snowfall than much of the Antarctic sea ice zone (Boisvert et al., 2020).

The optimization of this model is an under-constrained problem, likely with many local minima in goodness-of-fit metrics and thus many plausible "optimal" parameter sets. However, calibration is aided by the relative independence and intermittency of budget terms under different conditions. For example, only Q_{dep} adds significant snowfall (Q_{surf} provides negligible surface deposition) and only during reanalysis snowfall periods; only Q_{lead} scales with open-water fraction f_{OW}; Q_{rain} acts only during significant rainfall; Q_{melt} cannot be active simultaneously with Q_{rain} and applies only when $T_{\mathrm{a}} > T_{\mathrm{base}}$; and Q_{surf} and Q_{sub} are likewise mutually exclusive. Q_{dens} is the only process active continuously.

It is important to choose an optimization strategy suited to a model's characteristics. Some common techniques assume a near-linear response to varying parameters. The adjoint method, for example, requires a well-behaved tangent linear model (and a differentiable configuration), while a Green's function approach assumes a linear response to small perturbations. Our snow model, however, is highly nonlinear because parameterizations are intermittently active – triggered by episodic conditions – and state dependent, requiring snow to be present for loss to occur. This favors alternative optimization methods, including grid or random search strategies (Bergstra and Bengio, 2012) and more computationally efficient multi-armed bandit algorithms that focus resources on promising regions of the parameter space while balancing exploration with selection under uncertainty (Karnin et al., 2013). We adopt successive halving, a bandit-type framework common in machine learning in which

N candidate parameter sets are evaluated and the best-performing half are promoted to the next iteration, or rung, of the tuning ladder, while the remainder are discarded. The promoted set then defines the subsequent candidate batch, and so on until a stopping criterion or computational budget is reached (Karnin et al., 2013; Jamieson and Talwalkar, 2016).

Successive halving is implemented using candidate pools of $N = 54$ combinations of the eight tuning parameters for each rung (see Fig. 3 for the evolution of parameter values and goodness-of-fit metrics):

1. The algorithm is initialized in rung 0 with 54 parameter sets drawn from a one-sided truncated normal distribution on $(0.0, \infty)$ for all parameters except T_{base}, for which a standard normal distribution is used. Distributions are centered at 1.0 for each parameter (except T_{base} and γ_{melt}), with standard deviations chosen based on subjective assessment of the uncertainty in the underlying parameterizations (Table 2; including literature-based values for T_{base} and γ_{melt}). A 55th simulation is added in each rung using the baseline parameter set. A one-time simulation is also run with $\gamma_{\mathrm{new}} =$ 1.0 and all snow-loss parameterizations and mechanical compaction disabled (snow accumulation only).

2. For the baseline and 54 random parameter sets, the model is run in calibration mode with parcels evolving along snow buoy trajectories, driven by ERA5 and AMSR-E/2 SIC (Sect. 2.3).

3. Buoy observations are daily-averaged, and each buoy time series is shifted to align its initial snow depth with the corresponding model parcel. Goodness-of-fit metrics are then calculated between each ensemble member (including the baseline run) and the calibration and validation sets of buoy observations: root mean square error (RMSE) of snow accumulation, mean error (bias), and bias in daily snow accumulation tendency (after applying a 3 d rolling mean to buoy data to mitigate spikes).

4. The 27 parameter sets yielding the lowest RMSE against the calibration buoys are considered the top half of the ensemble. The median and standard deviation of each parameter across this top half define the baseline distributions used to generate the next rung's 54 parameter sets.

5. Steps (2)–(4) are repeated while ensemble-mean RMSE and/or baseline-run RMSE continue to improve (decrease) by at least 0.1 cm. From the final rung satisfying this criterion (rung 12), the median values of the five lowest-RMSE parameter sets are chosen as the final, optimized parameter set (Table 2).

6. Lastly, the model is run using the optimized parameter values to assess performance against the calibration and validation buoy sets.

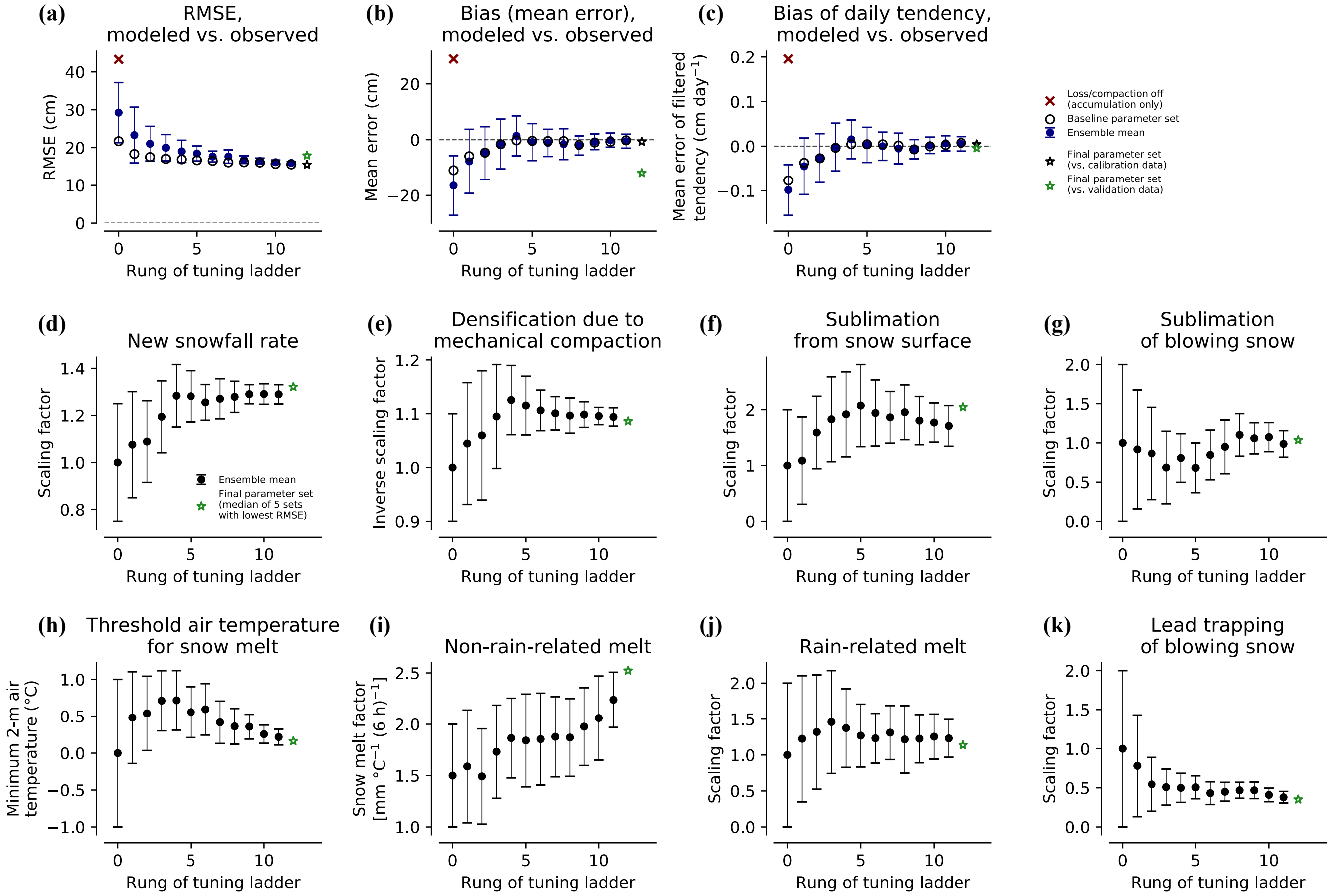

Figure 3. Evolution of the successive halving procedure used to optimize the model fit to snow buoy observations in the Weddell Sea. Each panel shows the ensemble distribution for 54 candidate parameter sets over the 12 iterations, or rungs, before the stopping criterion was reached. **(a)-(c)** Ensemble mean and standard deviation (blue) and values for the baseline parameter set (black open circles) of the RMSE of snow accumulation, bias of snow accumulation, and bias of daily snow accumulation tendency, respectively, comparing the model to the calibration set of buoys. The comparable values for an accumulation-only model run without loss or transformation processes are also marked (red crosses). Black and green stars, respectively, indicate the performance of the final optimized parameter set (the median of the five lowest-RMSE sets) assessed against the calibration and validation buoy measurements. **(d)-(k)** Ensemble median and standard deviation of the eight free parameter values over the tuning rungs. Green stars indicate final values from the optimized set.

3 Results and discussion

3.1 Model calibration and snow buoy observations

The final set of eight calibrated parameters yields a model RMSE of 15.5 cm, bias of –0.7 cm, and daily snow accumulation tendency bias of +0.004 cm d^{-1} relative to the matched Weddell Sea snow buoy measurements used for calibration (Fig. 3a–c). Against the independent validation set of buoys, the model shows an RMSE of 17.9 cm, bias of –12.0 cm, and tendency bias of –0.004 cm d^{-1}. The larger absolute bias in validation suggests a structural underestimation of snow accumulation that is masked by fitting to the calibration buoys, though this may also reflect differences across the buoy sets (see below). Nonetheless, the minimal tendency bias in both comparisons indicates that the model skillfully captures daily snow fluctuations owing to calibration (Fig. 3c), even if it may underestimate true snow accumulation over time due to accumulated biases.

The snow-accumulation-only simulation (with loss and mechanical compaction disabled; red crosses in Fig. 3a–c) yields a much higher RMSE of 43.3 cm and bias of 28.9 cm, illustrating the importance of these processes, while the pre-tuning simulation (rung 0) with all processes active yields an RMSE of 21.7 cm, bias of –11.0 cm, and tendency bias of –0.077 cm d^{-1}. Thus, calibration leads to a near-20-fold improvement in representing daily variability and an increase in net snow accumulation. Against the independent validation buoys, the untuned model exhibits a much larger bias of –30.9 cm (not shown in Fig. 3), suggesting that unexpected differences within the randomly split buoy data can explain much of the calibrated model's difficulty reproducing the validation buoy set. Overall, the tuned model potentially outperforms a commonly used passive microwave snow depth retrieval, for which comparison to Antarctic OIB data found an RMSE of 21 cm and bias of –19 cm – though a more robust retrieval method yielded an RMSE of 9 cm and bias of –2 cm (Shen et al., 2022). A caveat is that these data sources – buoy, airborne, model, and satellite – represent different spatial scales, from point measurements to multi-kilometer averages.

Overall, calibration increased net snow accumulation by scaling up new snowfall deposition ($\gamma_{\mathrm{new}} = 1.32$) and reducing the loss to leads during wind transport ($\gamma_{\mathrm{lead}} = 0.35$; Fig. 3d, k). This was partly compensated by increases in snow sublimation, densification, and both non-rain and rain-related melt after tuning. The more rapid and/or monotonic convergence of γ_{new} and γ_{lead} suggests these scaling factors are best constrained by the buoy observations. However, the notable changes in γ_{melt} and γ_{lead} are consistent with these parameterizations being most sensitive to unvalidated assumptions, including the degree-day melt approximation (Sect. 2.4.3) and the assumed relationship between open-water fraction and lead frequency (Sect. 2.4.6), respectively.

The need to increase snowfall input by 32 % suggests ERA5 may underestimate snowfall over the ice-covered Southern Ocean. For context, an average scaling factor of 1.58 for ERA5 snowfall in the Arctic Ocean was obtained by bias-correcting output from SnowModel-LG using OIB observations from 2009–2016 (Liston et al., 2020). In that study, however, other model parameters were not adjusted concurrently. This result contrasts with a CloudSat-based comparison suggesting ERA5 snowfall over the Arctic Ocean may be biased high, particularly in winter (Cabaj et al., 2020), and with a separate study finding minimal winter climatological bias relative to North Pole drifting-station records (Barrett et al., 2020). These divergent conclusions highlight the uncertainties arising from diverse validation data sets and techniques, as well as possible hemispheric differences.

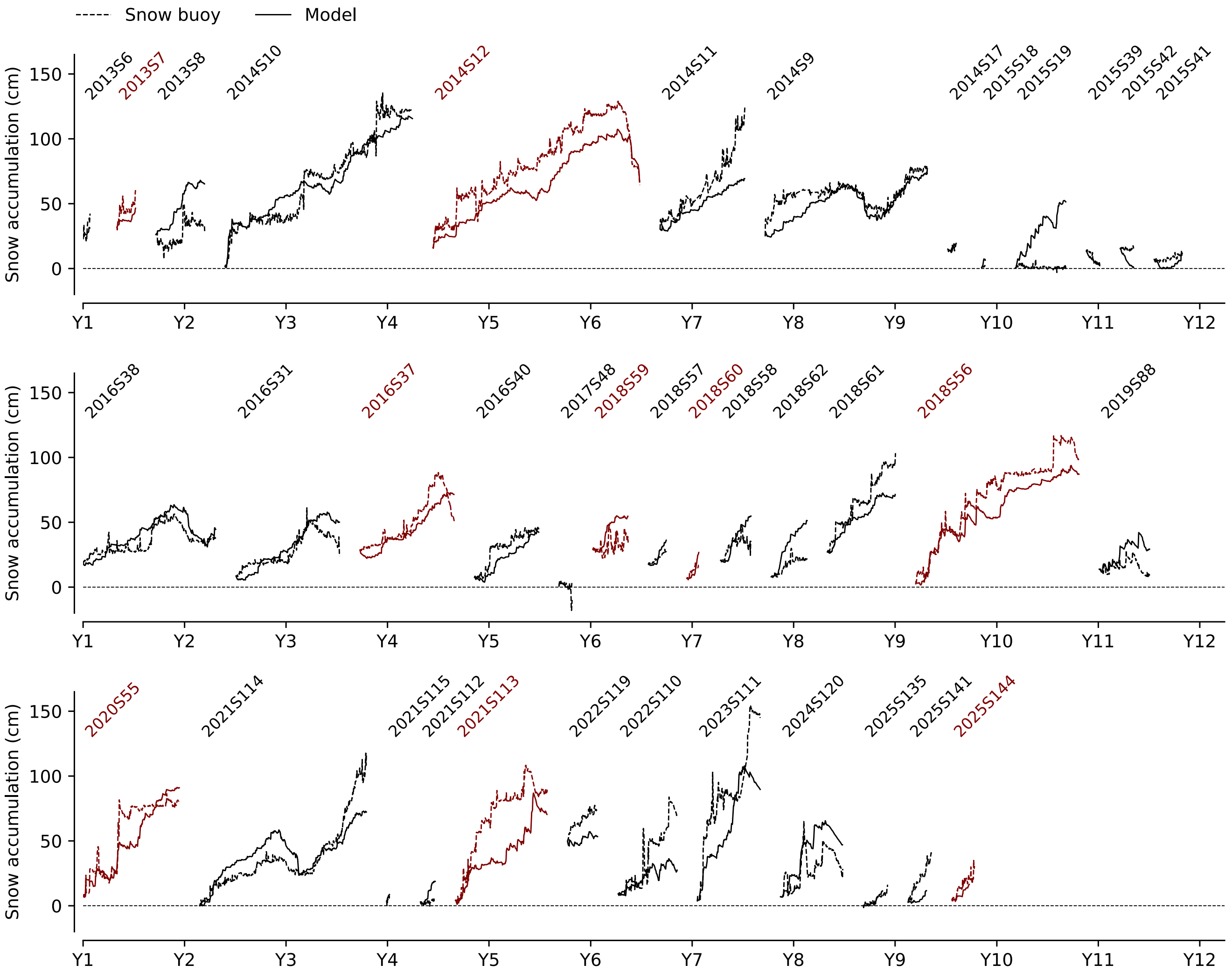

Figure 4. Model–buoy comparison after calibration of free parameters. Snow accumulation measured by the 39 snow buoys in the Weddell Sea (dashed lines) and reconstructed by the calibrated model along buoy trajectories (solid lines). Snow buoys are labeled with their IDs, which include the deployment year, with black indicating a buoy belonging to the calibration set and red denoting the validation set. For visualization purposes, the buoy measurements are depicted along a non-specific, continuous time axis in years.

Figure 4 compares the calibrated model evolution along snow buoy trajectories with the actual buoy measurements, showing broadly consistent temporal variability in many cases, though not all. The timing, if not always the magnitude, of major ablation events is often well captured, such as those near the end of the records for buoys 2014S12, 2016S38, and 2024S120. Because RMSE is the optimization metric, calibration may encourage over-correction, as possibly suggested by buoy 2021S114. That is, tuning may offset bias in one parameterization by introducing compensating bias in another to minimize divergence over time. Even so, this does not appear to be systematic across the model–buoy comparisons.

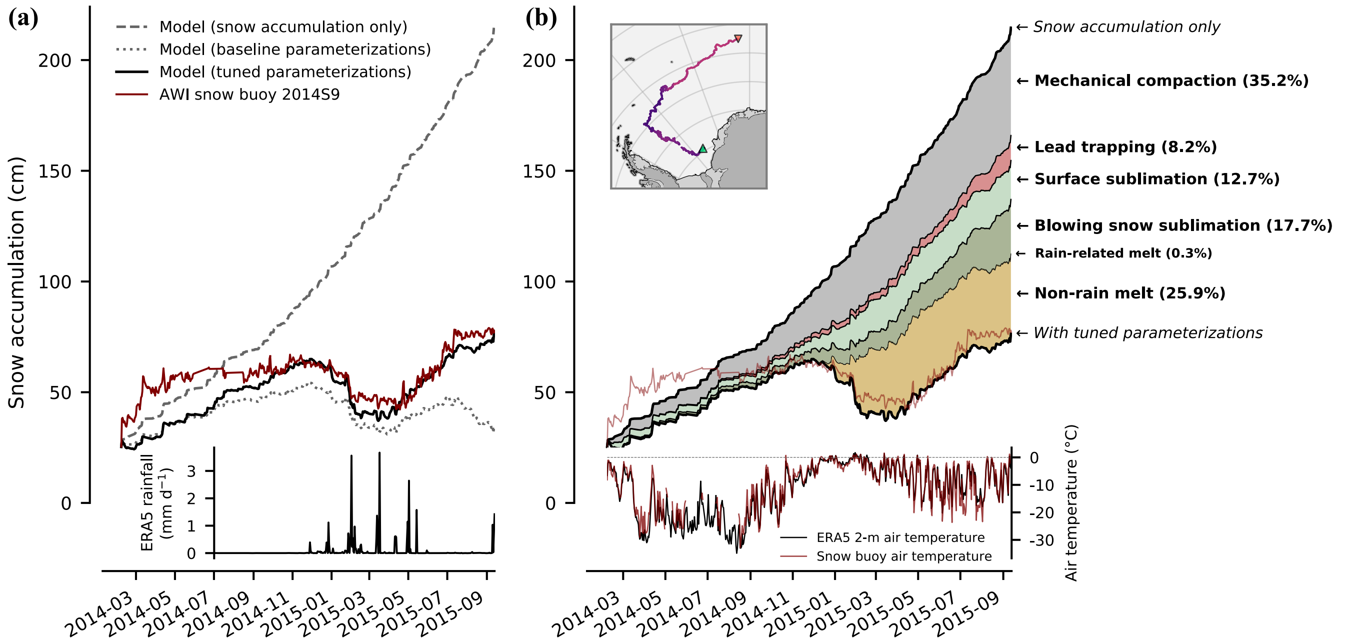

Figure 5. Observed and reconstructed snow accumulation along the trajectory of snow buoy 2014S9. **(a)** Buoy measurements (solid red line) and simulated evolution with loss processes and mechanical compaction disabled (dashed grey line), all parameterizations in their default configurations (dotted grey line), and the final calibrated model (solid black line). Daily ERA5 rainfall rates along the buoy trajectory are shown at bottom. **(b)** Partitioning of loss processes' cumulative contributions to the difference between the accumulation-only simulation and the full calibrated model. Daily air temperatures from ERA5 (black) and the buoy (red) are shown at bottom. The inset map shows the drift trajectory of buoy 2014S9, with colors indicating net snow accumulation (as in Fig. 1b) and green and red triangles marking the deployment location and last valid measurement.

A closer inspection of ~1.5 years of observations from buoy 2014S9 and the matched model simulations is illustrative (Fig. 5). The buoy was deployed in the southwest Weddell Sea and drifted northward then eastward, following the clockwise circulation of the Weddell gyre (triangle markers in Fig. 1b; inset in Fig. 5b). A deposition-only simulation – omitting loss processes and mechanical compaction – overestimates snow accumulation by more than a factor of 2, producing steady year-round growth (Fig. 5a). By contrast, the untuned full-physics simulation systematically underestimates snow accumulation, whereas the calibrated model reproduces much of the observed evolution. Observed snow depths exceed even the no-loss simulation in the initial months, suggesting underestimated ERA5 snowfall and/or unresolved small-scale redistribution; the calibrated simulation eventually catches up, possibly through over-correction.

It is tempting to infer causality from the apparent correspondence between rainfall and snow ablation events (Fig. 5a). Boisvert et al. (2020), analyzing the same buoy record, hypothesized that both ROS events and warm temperatures contributed to snow loss (their Figure 14). However, our parameterizations attribute nearly all ablation during these periods to the above-freezing air temperatures that tend to coincide with rain, with non-rain-related melt accounting for 25.9 % of cumulative snow loss – over 80 times larger than rain-related melt (Fig. 5b). Significant rain events are also more rare and brief than a daily time series suggests: buoy 2014S9, for example, experienced only 24 one-hour periods with ERA5 rainfall exceeding $R_{\mathrm{thresh}} = 0.25$ mm h^{-1}. The model's partitioning of loss mechanisms also highlights increasing lead trapping and blowing snow sublimation as the buoy approached the marginal ice zone (MIZ) late in its drift, the former likely reflecting higher open-water fraction.

Significant snow melt in early 2015 (Fig. 5b) is estimated to have produced 32 cm of superimposed ice, assuming complete refreezing of meltwater within the snowpack. This is uncommonly large relative to ice core observations from the northwestern Weddell Sea (Arndt et al., 2021), likely because this buoy spent an extended period at northern latitudes. The implied snow loss is equivalent to 42 % of the final snow depth. However, our model does not explicitly represent liquid-water effects such as melt metamorphism (Sect. 2.4.3); in actuality, meltwater infiltration would likely reduce the snow-only depth. Critically, the model also neglects snow-ice conversion following seawater flooding under heavy snow load (Sect. 3.3 and 3.5). Nonetheless, the mass budget of total meteoric freshwater (derived from snowfall and rainfall) should remain robust, despite uncertainties in conversion processes.

3.2 Climatological snow mass budget

Figure 6 depicts the climatological snow mass budget on Antarctic sea ice for 2003–2025, integrated over ice-covered areas. The apparent seasonality in new snowfall strongly resembles the seasonal cycle of Southern Hemisphere sea ice area or extent, indicating persistent year-round snowfall (Fig. 6a). Snow release to the ocean upon sea ice melt, by contrast, provides a freshwater pulse largely confined to spring and summer (September–February). Interannual variability in these two terms remains within a relatively narrow range when spatially averaged over such a large region. Blowing snow sublimation and lead trapping exhibit more muted seasonal cycles that mirror SIE, consistent with the wintertime prevalence of wind speeds strong enough to support aeolian transport. The persistence of lead trapping even in mid-winter reflects the presence of open water within the ice pack interior (Dubey et al., 2025), not only along the retreating spring ice edge. Most surface sublimation and non-rain melt occur over a shorter period, with the latter peaking after the December maximum in sea ice loss and snow release to the ocean, likely due to favorable snowpack energy balance conditions associated with elevated air temperatures and solar radiation.

The climatological mass budget closes to within 15 %, with total annual loss (9,812 Pg) exceeding new snow deposition (8,532 Pg; Fig. 6b). This residual reflects net depletion of snow originating from multiyear sea ice, which would manifest as model drift if simulations were run for multiple years. Even so, the small magnitude of the residual is notable given the lack of any explicit budget-closure constraint beyond the calibration procedure. Loss processes prior to complete sea ice melt – including melting and subsequent refreezing as superimposed ice – consume 39 % of annual snow mass (Fig. 6b). Among these, blowing snow sublimation contributes the most. Rain-related melt is negligible (<1 % of annual loss) compared to the 17 % from non-rain melt (see Sect. 3.1). Importantly, the large snow-release term includes snow converted into snow-ice, a process that incorporates seawater and is not simulated by our model. Consequently, "snow release" in this budget should be interpreted more broadly as a meteoric freshwater flux to the ocean.

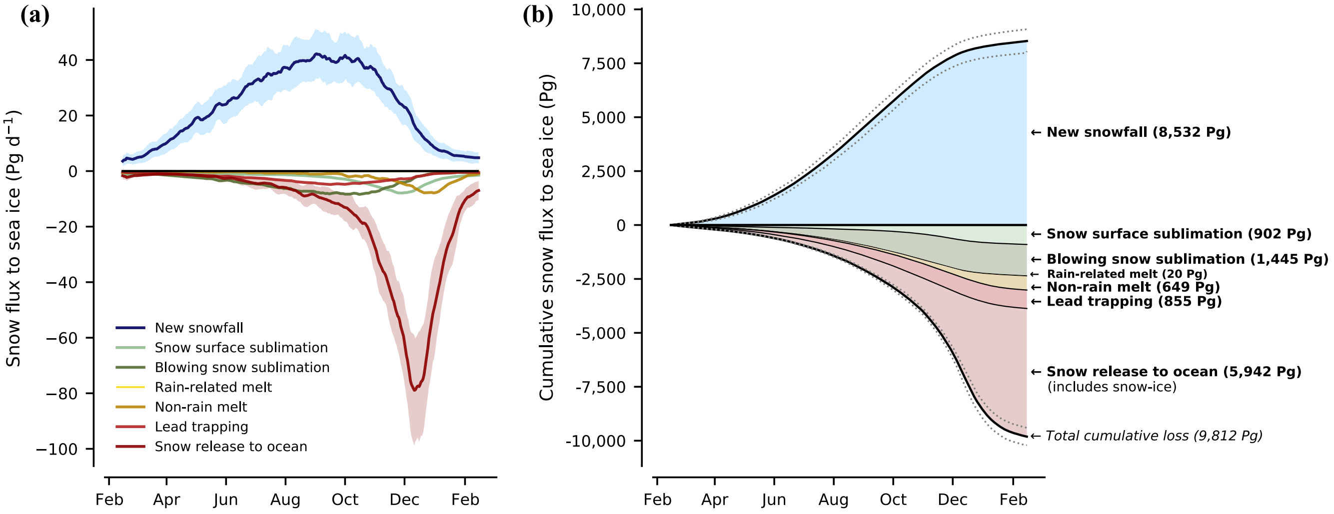

Figure 6. Climatological snow mass budget on Antarctic sea ice from the model reconstruction (2003–2025). The simulation period is February 15 to February 14 of the following year. **(a)** Climatological snow fluxes in Pg d^{-1} (1 Pg = 10^{12} kg), where positive values represent snow deposited on sea ice and negative values denote loss to either the atmosphere (surface and blowing snow sublimation), superimposed ice layer (rain-related and non-rain melt), or ocean (lead trapping and snow release upon sea ice melt, which includes snow converted to snow-ice). 7 d rolling mean values are shown for visualization purposes. Shading indicates the interannual variability of new snowfall and snow release to the ocean ($\pm 1\sigma$ over 2003–2025). **(b)** Cumulative fluxes over the model year, with totals listed at the right. Dotted grey lines indicate the interannual variability in the corresponding accumulated quantities ($\pm 1\sigma$). Note that rain-related melt is small and difficult to distinguish in both panels.

3.3 Freshwater fluxes

The amount, location, and timing of snow entering the ocean are integral to the salinity budget of the Southern Ocean, with implications for water mass transformation and vertical mixing (Kjellsson et al., 2015; Haumann et al., 2016; Pellichero et al., 2018; Wilson et al., 2019). Our model reconstruction estimates 270–311 mSv (1 mSv = 1,000 m^3 s^{-1}) of snowfall freshwater intercepted by sea ice, with the range bracketed by the model output and a budget fully balanced by loss. The total meteoric freshwater flux into the ocean originating from snow on sea ice is 237 mSv, representing 76–87 % of intercepted snowfall; the remainder sublimates to the atmosphere. This meteoric flux consists of 188 mSv released to the ocean upon complete sea ice melt, 21 mSv of primarily snowmelt-derived superimposed ice also released at melt (including a small contribution from rain), and 27 mSv delivered via lead trapping throughout the winter during wind-blown snow transport.

This meteoric ocean flux originating from snow intercepted by sea ice is equivalent to over half of the 410 ± 110 mSv annual freshwater flux from sea ice melt (excluding snow in snow-ice) across the Southern Ocean estimated by Haumann et al. (2016). In that study, remote sensing data were combined with a sea ice thickness reconstruction from a data-assimilating model to infer sea ice volume change and divergence. Haumann et al. also estimated 50 mSv of snow converted to snow-ice based on observational constraints on snow-ice prevalence compiled by Massom et al. (2001). Taken together with our model results, these estimates imply that ~21 % of the ice–ocean freshwater flux associated with snowfall onto sea ice is in the form of snow-ice, though this calculation is approximate.

Our snow-related freshwater fluxes are qualitatively consistent with an observation-based estimate – albeit with significant simplifying assumptions – that precipitation (onto sea ice *and* directly into the ocean, including areas without ice cover) and sea ice freshwater fluxes each contribute comparably to buoyancy gain in the Southern Ocean sea ice sector (Pellichero et al., 2018; see their Supplementary Note 2). This contrasts with Abernathey et al. (2016), who used the Southern Ocean State Estimate (SOSE; Mazloff et al., 2010), which assimilates ocean temperature and salinity, sea ice concentration, and other observational data to constrain MITgcm. The model's ocean state is adjusted via the adjoint method, which can alter atmospheric forcing such as precipitation. Abernathey et al. report annual freshwater fluxes of 140 mSv from snowfall intercepted by Antarctic sea ice and 360 mSv from sea ice freezing and melting, with the latter excluding melt of overlying snow and the snow-derived fraction of snow-ice. This SOSE snowfall estimate is only 45–52 % of the intercepted snowfall from our calibrated, reanalysis-driven reconstruction, suggesting that the adjoint method may have compensated for biases in simulated sea ice or ocean physics by substantially reducing snowfall forcing relative to reanalysis. Such an adjustment could preserve agreement with ocean observations while masking excessive sea ice melt in MITgcm, implying overestimated sea ice formation rates and thickness. Consistent with this interpretation, Abernathey et al. report that SOSE sea ice thickness is 20–40 cm too thick in the Weddell and Ross seas, a common positive bias in coupled models (Holland et al., 2014). Similarly, Nakayama et al. (2024) identify a summer fresh-surface bias in the biogeochemical version, B-SOSE, linked to an overly strong sea ice seasonal cycle.

These uncertainties highlight the importance of accurately partitioning Southern Ocean freshwater fluxes between snow and sea ice in coupled models. A freshwater input that is correct in total but contains an unrealistically low proportion of snow may require higher sea ice melt and growth rates to compensate, which has implications for brine rejection and stratification near the Antarctic margin where sea ice formation is greatest.

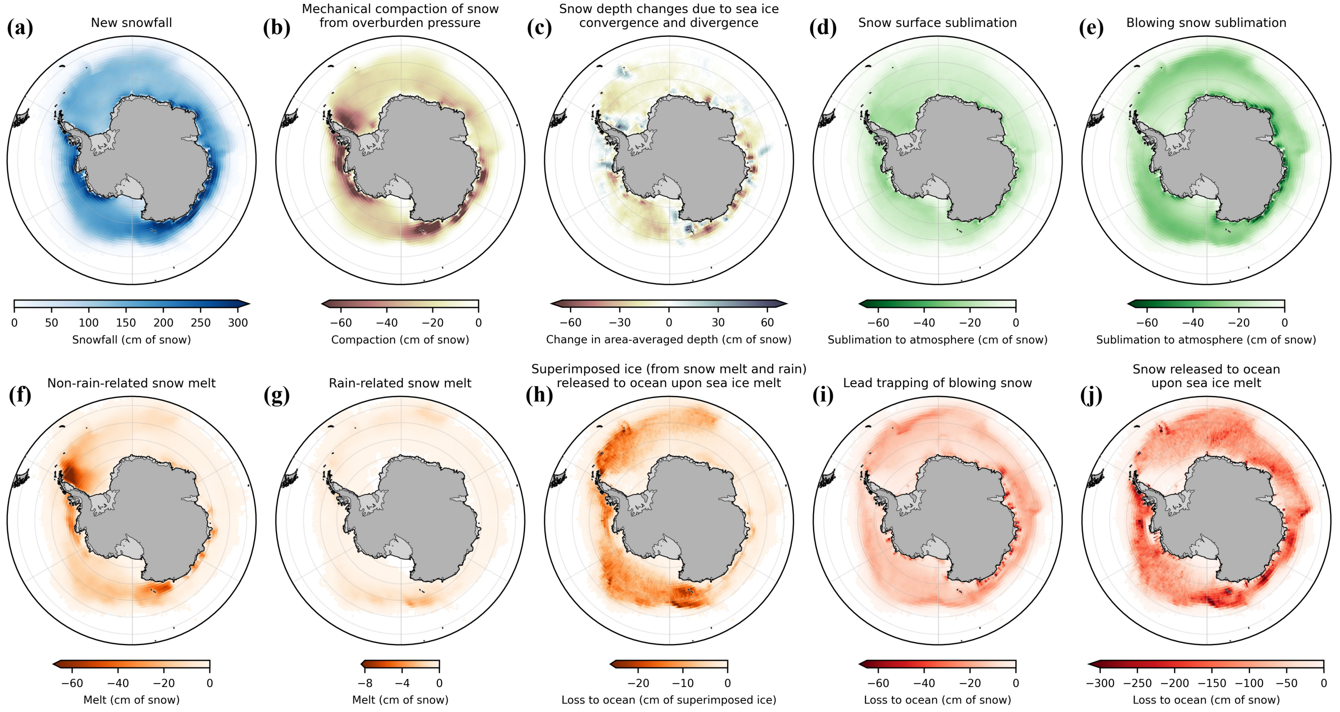

Figure 7. Average annual contributions to the net snow accumulation budget on sea ice in the model reconstruction (2003–2025). Positive values indicate greater net snow accumulation. All contributions except panel **[h]** are expressed as changes in snow depth, normalized from their time-varying bulk snow density to $\rho_{s,0} = 320$ kg m^{-3}. The color groupings correspond to the fate of snow: blue signifies snow deposition onto sea ice; diverging pink and blue-grey represent mass-conserving decreases and increases in area-averaged snow thickness, respectively; green denotes sublimation to the atmosphere; orange includes snow melt and superimposed ice formed from snow melt and rain (note that panel **[h]**, showing superimposed ice released to the ocean, is not part of the snow accumulation budget); and red represents direct snow flux to the ocean, with panel **[j]** including snow converted to snow-ice. Note that color scales are not uniform, as reflected in the different colorbar lengths.

3.4 Spatial distribution of snow accumulation and loss processes

Figure 7 illustrates spatial patterns in reconstructed snow fluxes, presented as annual contributions to the net snow accumulation budget averaged over 2003–2025. Snowfall deposition of ~1–2 m occurs across the ice-covered Southern Ocean, with higher deposition along the continental margin, particularly off East Antarctica and the Amundsen Sea–Bellingshausen Sea coastline (Fig. 7a). This pattern broadly aligns with CloudSat-derived snowfall estimates, though these encompass both ice-covered and ice-free periods (Boisvert et al., 2020).

As expected, mechanical compaction is most pronounced along the coastline where net snow accumulation is high (Figs. 7b and 8a). Although compaction is mass conserving and thus excluded from the snow mass budget, it reduces snow depth by ~20 cm or more across the sea ice region. Large-scale sea ice divergence contributes to area-averaged snow thinning within the Weddell and Ross gyres (Fig. 7c), where ice-concentration budget analyses indicate that divergent ice drift supports formation of new, snow-free ice (Holland and Kwok, 2012; Holland and Kimura, 2016). In areas of convergence and simulated snow thickening, snow depth may remain relatively unchanged in reality because snow can be flooded and frozen into snow-ice or lost to the ocean during sea ice ridging (Sect. 2.4.7). However, our reconstruction identifies only limited regions of convergence, primarily in the Bellingshausen Sea and western Weddell Sea, suggesting that these impacts are spatially restricted (Fig. 7c).

Blowing snow sublimation exhibits higher rates at northern latitudes and a narrow band of intense sublimation along the East Antarctic coast, likely driven by strong winds and dry, subsaturated katabatic outflow from the Antarctic continent (Fig. 7e). This differs somewhat from a previous estimate by Déry and Yau (2002), who applied the same parameterization to coarser, uncalibrated ERA-15 reanalysis (1979–1993). Their results show more fragmented coastal maxima and a pronounced hotspot in the northern Ross Sea that is less prominent in our estimates. In contrast, snow surface sublimation is spatially diffuse and weaker, both in our reconstruction (Fig. 7d) and in Déry and Yau (2002). Fichefet and Morales Maqueda (1999) estimated up to 0.45 m per year of snow removal by surface sublimation – substantially higher than our reconstruction, though potentially comparable if blowing snow (absent from their model) were included. They further noted that conditions over Antarctic sea ice may favor snow sublimation relative to the Arctic because drier air and stronger winds produce latent heat fluxes that are 3 times higher on average.

Hotspots of non-rain melt are evident in the Bellingshausen Sea, western Weddell Sea, offshore of the Wilkes Basin, and broadly across the Ross Sea (Fig. 7f). The western Weddell Sea and Wilkes Basin maxima coincide with key cyclogenesis regions inferred from storm tracks over the Southern Ocean (Yuan et al., 2009), consistent with episodic warm-air transport. Superimposed ice formed during these snow ablation events is advected downstream along ice-drift trajectories (Fig. 1a) and is subsequently released to the ocean in the northern Weddell and Ross gyres and farther north offshore of the Wilkes Basin (Fig. 7h).

Although lead trapping and snow release upon complete sea ice melt differ greatly in magnitude, both show strongest losses concentrated near the sea ice edge (Fig. 7i, j). These patterns in freshwater fluxes, however, likely arise from distinct mechanisms: high lead trapping in the MIZ follows from the increased open-water fraction in this dynamic region, whereas the concentration of snow release reflects intense melt of snow-covered ice transported from higher latitudes. For context, Eicken et al. (1994) estimated ~10 cm SWE per year of snow lost to leads in the Weddell Sea using simple empirical relations to wind speed. This corresponds to ~31 cm of snow, roughly twice our circumpolar estimate, in which lead trapping in the Weddell Sea is not anomalously higher than other regions. Leonard and Maksym (2011) proposed that about half of September snowfall on Antarctic sea ice may be lost to leads, an order-of-magnitude estimate that likewise contrasts with our reconstruction estimate of 855 Pg per year, just 9 % of the annual snow mass budget (Fig. 6b).

To our knowledge, our lead-trapping reconstruction (Sect. 2.4.6) is the most sophisticated yet implemented in a large-scale model of snow on sea ice. It incorporates a nonlinear wind-speed dependence and a linear dependence on open-water fraction, with the wind speed relationship derived from two-dimensional boundary-layer simulations. It also uses a well-validated, temperature-dependent threshold for aeolian snow transport and calibrates lead trapping concurrently with other loss mechanisms. By comparison, previous work has adopted simpler approaches: lead trapping restricted to the time of initial snow deposition, a fixed fraction of snowfall diverted to the ocean, a fixed wind speed threshold, and/or an assumed linear dependence on wind speed (Fichefet and Morales Maqueda, 1999; Lecomte et al., 2013, 2015; Petty et al., 2018).

In contrast to these approaches and our simulation, the SnowModel-LG reconstruction for Arctic sea ice (Liston et al., 2020) does not represent lead trapping. Liston et al. argue this process is likely unimportant in the Arctic due to several factors: rapid refreezing of leads, lower lead frequency relative to blowing snow erosion length scales, more effective snow capture by surface roughness elements than by leads, lock-up effects (see Sect. 2.4.5), and limited snow transport in the moisture-rich MIZ. While these arguments may find validation in the scaling down of our lead trapping parameterization to 35 % of its original magnitude during calibration (Sect. 3.1), their applicability to Antarctic sea ice conditions is uncertain. Compared to the Arctic, leads are more prevalent in the Southern Ocean, associated with strong currents and bathymetry (Dubey et al., 2025) and predominantly divergent ice drift (Holland and Kwok, 2012). Moreover, higher ocean heat fluxes (e.g., Martinson and Iannuzzi, 1998; Lytle and Ackley, 2001) may permit more melting of snow trapped in leads. Field observations are sparse, but Leonard and Maksym (2011) report near-total snow loss to leads during a three-week Bellingshausen Sea drift experiment. Even in the Arctic, field observations show that lead trapping can be substantial under warmer air temperatures that maintain open water, whereas typical winter conditions may yield only minimal snow loss to leads (Clemens-Sewall et al., 2023).

3.5 Snow depth, snow-ice formation, and bulk snow density

It is important to distinguish between snow accumulation and snow depth, which we treat as distinct metrics. Snow depth, measured using snow cores or pits on sea ice or estimated remotely using radar altimetry or passive microwave radiometry, excludes any basal snow layer that has been converted into ice. On the other hand, net snow accumulation, as simulated by our model, likewise reflects the balance of snow mass gain and loss to the atmosphere and ocean but accounts for only one conversion pathway: formation of superimposed ice from snow melt, albeit represented simplistically (Sections 2.4.3 and 3.1).

The WASSAIL model does not simulate snow-ice formation, a key conversion process in which the snowpack becomes flooded by seawater and freezes into a new layer of ice. Ice core measurements suggest snow-ice constitutes 8–38 % of total ice thickness, with strong regional and seasonal variations around Antarctica (Massom et al., 2001). Snow-ice formation is most prevalent where snow deposition is high and ice remains thin, a situation conducive to the isostatic depression of ice freeboard below sea level (Webster et al., 2018). In an analysis of Weddell Sea snow buoys that inferred sea ice growth using a one-dimensional thermodynamic model, Arndt et al. (2024) estimated an average maximum snow-ice thickness of 16 cm across 36 buoys. This process is less common in the Arctic, with exceptions during strong storm events (e.g., Merkouriadi et al., 2017). Sea ice deformation under convergent drift and wave overwash may also promote snow-ice formation in parts of the Southern Ocean (e.g., Massom et al., 1998).

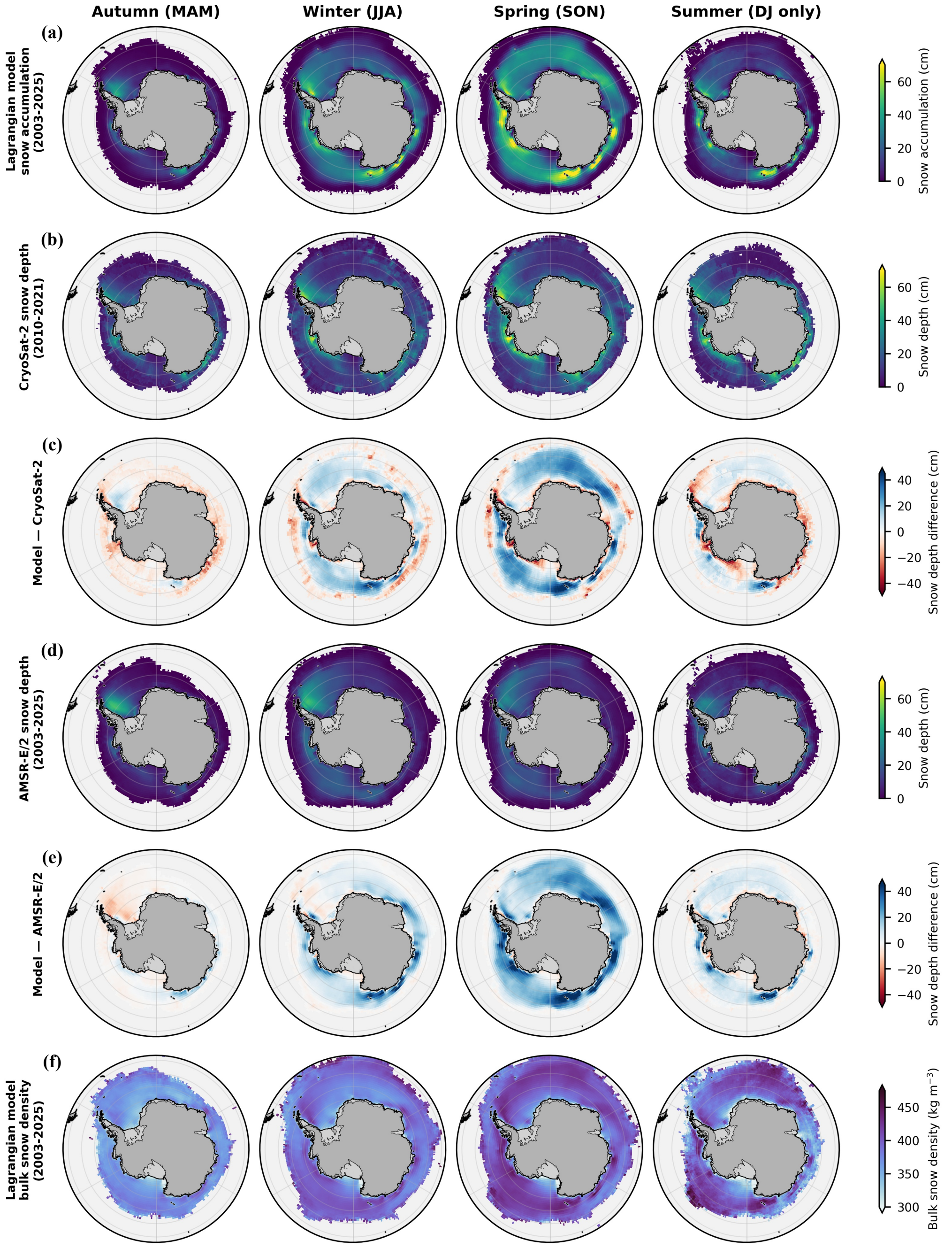

Figure 8. Comparisons between the WASSAIL model reconstruction (2003–2025) and snow depth from two remote sensing products. Columns are averages for autumn (March/April/May), winter (June/July/August), spring (September/October/November), and summer (December/January only, as the model is initialized and terminated in mid-February). **(a)** Simulated net snow accumulation. **(b)** Snow depth on sea ice from a monthly CryoSat-2 retrieval from July 2010–August 2021 (Fons et al., 2023). **(c)** Differences between the reconstructed snow accumulation and CryoSat-2-based snow depths. **(d)** Snow depth estimated from AMSR-E and AMSR2, averaged from daily data from 15 February 2003–14 February 2025 (Cavalieri et al., 2014; Meier et al., 2018). **(e)** Differences between reconstructed snow accumulation and AMSR-E/2 snow depths. **(f)** Model reconstruction of bulk snow density.

With these distinctions in mind, Figure 8 compares snow accumulation from WASSAIL with snow depth from two remote sensing products, shown as seasonal climatological averages. The model reconstruction yields circumpolar mean net snow accumulation of 11.5 cm in autumn, 21.3 cm through winter, 30.9 cm through spring, and 22.7 cm through summer, based on daily spatial averages within ice-covered areas (Fig. 8a). Spatial patterns are generally diffuse but include regions of markedly higher snow accumulation (~60 cm or more by spring) in the western Weddell Sea, the Bellingshausen Sea, along the Amundsen Sea coast, and along the East Antarctic margin from Queen Mary Land eastward. These hotspots persist into summer despite widespread ice melt and snow ablation across the sea ice zone. Thick snow in the western Weddell Sea coincides with dynamical thickening from convergent ice motion (Fig. 7c). Elsewhere, these hotspots align closely with areas of elevated snowfall (Fig. 7a), with patterns slightly broadened by ice drift (Fig. 1a).

Comparing our model's net snow accumulation with snow depth retrievals based on CryoSat-2 radar altimetry (Fons et al., 2023; Sect. 2.2.2) and AMSR-E/2 passive microwave radiometry (Cavalieri et al., 2014; Meier et al., 2018; Sect. 2.1.2) demonstrates the difference between snow accumulation and depth (Fig. 8b–e). Subtracting the satellite retrievals from the model fields reveals positive differences of ~20–30 cm across much of the sea ice zone by spring, which we interpret as evidence of widespread snow-ice formation of that magnitude. This inferred conversion of snow to snow-ice corresponds to 49 % (CryoSat-2) or 60 % (AMSR-E/2) of net springtime snow accumulation (September–November), averaged over regions with positive differences in each comparison, with the caveat that CryoSat-2 represents a different period (2010–2021).

Interpreting the differences in Fig. 8c as indicative of snow-ice formation aligns with observations suggesting that the process is ubiquitous across the Southern Ocean, including the central Weddell Sea and the Amundsen–Bellingshausen seas (Eicken et al., 1994; Massom et al., 1997, 2001; Sturm et al., 1998). Ice cores from the Ross and Amundsen–Bellingshausen sectors indicate that snow-ice conversion reduces net snow accumulation by 30–58 % (Jeffries et al., 2001), comparable to our inferred fractions. The seasonality of the model–satellite differences, peaking in September–November, is also consistent with snow-ice formation typically beginning in the latter half of winter as snow loads increase while ice growth slows (Eicken et al. 1995; Singh et al. 2021), with Southern Ocean snow-ice volume reaching a maximum in November (Fichefet and Morales Maqueda, 1999).

A similar approach for inferring snow-ice formation was used by Maksym and Markus (2008), who reconstructed snow accumulation from ice motion and ERA-40 reanalysis snowfall and interpreted accumulation exceeding passive microwave snow depth as snow-ice conversion. Although their reconstruction omitted other loss processes and likely overestimated accumulation off East Antarctica due to ERA-40 snowfall biases, their September snow-ice thickness estimates (their Figure 7) align remarkably well in both magnitude and spatial pattern with the calculated difference between our simulated snow accumulation and AMSR-E/2 snow depth (Fig. 8e). However, this correspondence is less robust for CryoSat-2 (Fig. 8c), highlighting the sensitivity of this approach to the choice of satellite snow depth product.

Our reconstruction also yields the seasonal evolution of bulk snow density, with a circumpolar mean of 357 kg m^{-3} in autumn increasing to 381 kg m^{-3} in winter and 399 kg m^{-3} in spring, then returning to 371 kg m^{-3} in summer (Fig. 8f). This seasonality reflects two parameterized processes: wind-enhanced compaction of fresh snowfall, which determines the density of a new snow layer based on the first 100 h of post-deposition wind speeds that it experiences, and mechanical compaction under overburden pressure. Spatially, bulk snow density tends to be lower at higher latitudes, consistent with thinner, less compacted snow on newly formed ice near the continent (Fig. 1a) and lower new-snow densities owing to weaker winds. This pattern is supported by an approximately linear decrease in zonal-mean ERA5 10 m wind speed from 55° S to 80° S across all seasons (not shown).

Our estimates of bulk snow density are somewhat higher than in situ observations that show, for example, mean winter densities of 320 kg m^{-3} and 360 kg m^{-3} from snow pits in the Weddell Sea and Indian Ocean sectors, respectively, though variability across locations is large (Massom et al., 2001). One contributing factor may be excessive compaction rates because the model does not remove snow from the column via snow-ice formation. In any case, the magnitude of spatial variability in reconstructed bulk snow density appears comparable to its seasonal variability. This suggests that adopting only temporally varying snow density, as in some circumpolar modeling and remote sensing efforts (e.g., Kurtz and Markus, 2012; Fons et al., 2023; Lawrence et al., 2024), may be an oversimplification given regional differences in dominant snow processes across the Southern Ocean.

4 Conclusions

In this study, we present the conceptual framework, method, and results of a reconstruction of snow on Antarctic sea ice that is among the most comprehensive to date. Our model, WASSAIL, occupies a middle ground between high-complexity, multilayer snow evolution models such as SnowModel-LG (Liston et al., 2020) – which simulates snowpack thermodynamics and redistribution processes but has been applied only to the Arctic Ocean – and simpler reconstruction models (Maksym and Markus, 2008; Blanchard-Wrigglesworth et al., 2018; Petty et al., 2018; Lawrence et al., 2024), which generally prioritize interpretability and the ability to use calibration techniques (e.g., Cabaj et al., 2023). WASSAIL combines elements of both approaches by incorporating a more rigorous treatment of key snow-on-sea-ice processes while remaining computationally efficient, which enables future sensitivity experiments and possible implementation of its parameterizations into global climate models.

The model's core process parameterizations (except for rain-related melt) all appear to influence the fate of intercepted snow, of which over one-third is lost prior to seasonal ice melt. Several of these erosion and transformation processes – particularly those involving wind-blown snow and density compaction – are absent from many coupled climate models, where snow density is often prescribed rather than treated as a prognostic variable. At the same time, considerable uncertainties remain as to the magnitudes and mechanisms of these processes, especially lead trapping. Our model neglects several potentially influential but poorly constrained processes that are challenging to represent accurately, including the metamorphic effects of liquid water and the role of snow age in diagenetic lock-up. Critically, snow-ice conversion is not explicitly represented; instead, we estimate it by subtracting satellite snow depth retrievals from reconstructed snow accumulation. Because snow-ice formation constitutes a major component of the coupled snow–sea ice mass budget, reconstructions like ours cannot be used to evaluate remote sensing estimates of snow depth without accounting for this conversion process using independent constraints on sea ice thickness.

Despite these limitations, the reconstructed snow mass budget is a useful tool for clarifying the importance of snow in the Antarctic ice–ocean system. For example, the potential role of lead trapping in the mixed-layer salinity budget has largely gone unaddressed in the oceanographic literature, which typically assumes snow is not available for release until spring melt (e.g., Gordon et al., 1984; Martinson and Iannuzzi 1998). Snow-derived freshwater fluxes influence upper-ocean stratification, which may in turn modulate interannual variability in Antarctic sea ice (Goosse and Zunz, 2014), making a realistic accounting of the timing and magnitude of snow fluxes essential. Neglecting snow loss processes can also result in excessive snow accumulation and snow-ice formation, accompanied by spurious brine rejection into the upper ocean. Such biases could plausibly erode stratification in regions already prone to convective overturning (Kjellsson et al., 2015; Campbell et al., 2019; Wilson et al., 2019) or exacerbate ice melt by promoting entrainment of warm pycnocline waters. This dynamic could also artificially strengthen the "conveyor belt" behavior whereby Antarctic sea ice, on occasion, grows from the top via snow flooding while melting at its base due to elevated ocean heat fluxes (Lytle and Ackley, 2001; Maksym et al., 2012).

Ultimately, Antarctic sea ice acts as a dynamic catchment basin for snowfall over the Southern Ocean, intercepting and funneling it toward hotspots of sea ice melt. We find that snow on sea ice supplies an annual meteoric freshwater flux to the ocean equivalent to more than half of the circumpolar freshwater flux from sea ice melt (Haumann et al., 2016). Our estimate – about twice that of a widely used data-assimilating ocean state estimate (Abernathey et al., 2016) – highlights the powerful role of sea ice as a spatial and temporal filter that transports snow equatorward and delays most snow release until spring melt, while permitting some earlier loss to lead trapping (as well as ridging). This filtering process likely influences Southern Ocean water mass transformation in profound ways: snow input adds buoyancy to upwelled deep waters destined for lower latitudes, while northward export of intercepted snow away from the Antarctic margin facilitates the densification of bottom-water precursors, helping to sustain the global overturning circulation (Talley, 2008; Lago and England, 2019). The apparent new, lower trajectory of Antarctic sea ice (Purich and Doddridge, 2023) raises questions about how the overlying snow cover will respond to – and shape – this ongoing transition in the Southern Ocean.

Appendix A

Table A1: Coefficients for Q'_{sub} in Eq. (24), reproduced from Déry and Yau (2001).

Coefficient	Value
a_0	3.78407×10^{-1}
a_1	-8.64089×10^{-2}
a_2	-1.60570×10^{-2}
a_3	7.25516×10^{-4}
a_4	-1.25650×10^{-1}
a_5	2.48430×10^{-2}
a_6	-9.56871×10^{-4}
a_7	1.24600×10^{-2}
a_8	1.56862×10^{-3}
a_9	-2.93002×10^{-4}

Table A2: Latent heat of condensation L and thermal conductivity and diffusion coefficients K and D adapted from Rogers and Yau (1989), 815 Tables 2.1 and 7.1.

T_a (°C)	L (J g^{-1})	K (J m^{-1} s^{-1} K^{-1})	D (m^2 s^{-1})
–40	2603	2.07×10^{-2}	1.62×10^{-5}
–30	2575	2.16×10^{-2}	1.76×10^{-5}
–20	2549	2.24×10^{-2}	1.91×10^{-5}
–10	2525	2.32×10^{-2}	2.06×10^{-5}
0	2501	2.40×10^{-2}	2.21×10^{-5}
5	2489	-	-
10	2477	2.48×10^{-2}	2.36×10^{-5}
15	2466	-	-
20	2453	2.55×10^{-2}	2.52×10^{-5}
25	2442	-	-
30	2430	2.63×10^{-2}	2.69×10^{-5}

Table A3: Simulated rate of blowing snow lost to a lead with fetch (width) of 1 km after transport over 1 km of sea ice, reproduced from Déry and Tremblay (2004), Table 1, in relation to 10 m wind speed.

U_{10} (m s^{-1})	Q'_{lead} (mm SWE d^{-1})
10	12.5
15	16.2
20	29.1
25	66.0

Code and data availability

Daily gridded WASSAIL model output fields from 2023–2025 are available at https://doi.org/10.5281/zenodo.19507961 (Campbell, 2026a). The Python code used to run the model and generate the analyses and figures presented here can be accessed at https://github.com/ethan-campbell/WASSAIL/ and is archived at https://doi.org/10.5281/zenodo.19509689 (Campbell, 2026b). All data used in this study are publicly available. The AMSR-E and AMSR2 sea ice concentration data are available from University of Bremen (last access: 20 April 2025) at https://seaice.uni-bremen.de/sea-ice-concentration/amsre-amsr2/ (Spreen et al., 2008). The CDR and CDR-NRT sea ice concentration data are available from NSIDC (last access: 21 April 2025) at https://doi.org/10.7265/rjzb-pf78 and https://doi.org/10.7265/j0z0-4h87, respectively (Meier et al., 2024a, b). The AMSR-E and AMSR2 snow depth on sea ice retrievals are available from NSIDC (last access: 20 April 2025) at https://doi.org/10.5067/AMSR-E/AE_SI12.003 and https://doi.org/10.5067/RA1MIJOYPK3P, respectively (Cavalieri et al., 2014; Meier et al., 2018). Polar Pathfinder sea ice motion data are available from NSIDC (last access: 21 April 2025) at https://doi.org/10.5067/INAWUWO7QH7B and https://doi.org/10.5067/O0XI8PPYEZJ6 (Tschudi et al., 2019a, b). The ECMWF ERA5 atmospheric reanalysis fields are available from the Copernicus Climate Change Service (last access: 24 April 2025) at https://doi.org/10.24381/cds.adbb2d47 (Copernicus Climate Change Service, 2023). The snow buoy measurements are available from AWI (last access: 1 May 2025) at https://data.meereisportal.de/relaunch/buoy.php (Nicolaus et al., 2017). The CryoSat-2 snow depth estimates are available on Zenodo at https://doi.org/10.5281/zenodo.7327711 (Fons et al., 2023).

Author contributions

ECC designed the study, developed the model, performed the simulations and analyses, produced the figures, and prepared the manuscript. SCR acquired funding, supervised the project, and provided input to the manuscript. MAW contributed to the interpretation of results and provided input to the manuscript.

Competing interests

The contact author has declared that none of the authors has any competing interests.

Acknowledgements

We thank David Darr for computational support and Alek Petty, Cecilia Bitz, Eric D'Asaro, Georgy Manucharyan, and Eric Steig for their useful feedback over the course of this project. We also acknowledge the participants of the Physical Oceanography Dissertation Symposium (PODS) XIII for insightful discussions. We extend our deep appreciation to those involved in the Alfred Wegener Institute's snow buoy program and the RV *Polarstern* cruises on which snow buoys were deployed, which enabled the calibration and validation of this model reconstruction.

Financial support

ECC acknowledges funding from the US Office of Naval Research through the National Defense Science & Engineering Graduate (NDSEG) Fellowship Program; the National Science Foundation (NSF) through the Southern Ocean Carbon and Climate Observations and Modeling (SOCCOM) Project (PLR-1425989 and OPP-1936222), Global Ocean Biogeochemistry Array (GO-BGC) Project (OCE-1946578), and an Office of Polar Programs Postdoctoral Research Fellowship (OPP-2420300); and the National Oceanic and Atmospheric Administration through award NA20OAR4320271. MAW acknowledges funding from the National Aeronautics and Space Administration's ICESat-2 program (1699716).

References

Abernathey, R. P., Cerovečki, I., Holland, P. R., Newsom, E., Mazloff, M., and Talley, L. D.: Water-mass transformation by sea ice in the upper branch of the Southern Ocean overturning, Nat. Geosci., 9, 596–601, https://doi.org/10.1038/ngeo2749, 2016.

Abolafia-Rosenzweig, R., He, C., Chen, F., and Barlage, M.: Evaluating and enhancing snow compaction process in the Noah-MP Land Surface Model, J. Adv. Model. Earth Syst., 16, e2023MS003869, https://doi.org/10.1029/2023MS003869, 2024.

von Albedyll, L., Haas, C., and Dierking, W.: Linking sea ice deformation to ice thickness redistribution using high-resolution satellite and airborne observations, Cryosph., 15, 2167–2186, https://doi.org/10.5194/tc-15-2167-2021, 2021.

Anderson, E. A.: NOAA Technical Memorandum NWS-HYDRO-17: National Weather Service river forecast system – Snow accumulation and ablation model, National Oceanic and Atmospheric Administration, 1973.

Anderson, E. A.: NOAA Technical Report NWS 19: A point energy and mass balance model of a snow cover, National Oceanic and Atmospheric Administration, 150 pp., 1976.

Anderson, E. A.: Snow accumulation and ablation model – SNOW-17, National Weather Service, 2006.

Andreas, E. L., Persson, P. O. G., Jordan, R. E., Horst, T. W., Guest, P. S., Grachev, A. A., and Fairall, C. W.: Parameterizing turbulent exchange over sea ice in winter, J. Hydrometeorol., 11, 87–104, https://doi.org/10.1175/2009JHM1102.1, 2010.

Arndt, S. and Paul, S.: Variability of winter snow properties on different spatial scales in the Weddell Sea, J. Geophys. Res. Ocean., 123, 8862–8876, https://doi.org/10.1029/2018JC014447, 2018.

Arndt, S., Haas, C., Meyer, H., Peeken, I., and Krumpen, T.: Recent observations of superimposed ice and snow ice on sea ice in the northwestern Weddell Sea, Cryosph., 15, 4165–4178, https://doi.org/10.5194/tc-15-4165-2021, 2021.

Arndt, S., Maaß, N., Rossmann, L., and Nicolaus, M.: From snow accumulation to snow depth distributions by quantifying meteoric ice fractions in the Weddell Sea, Cryosph., 18, 2001–2015, https://doi.org/10.5194/tc-18-2001-2024, 2024.

Arndt, S., Webster, M., Sturm, M., and Massom, R. A.: Snow on sea ice and how it varies through the seasons, in: Sea Ice, 4th ed., edited by: Thomas, D. N., John Wiley & Sons, Ltd, Hoboken, NJ, 41–112, https://doi.org/10.1002/9781394213764.ch02, 2025.

Barrett, A. P., Stroeve, J. C., and Serreze, M. C.: Arctic Ocean precipitation from atmospheric reanalyses and comparisons with North Pole drifting station records, J. Geophys. Res. Ocean., 125, e2019JC015415, https://doi.org/10.1029/2019JC015415, 2020.

Bergstra, J. and Bengio, J.: Random search for hyper-parameter optimization, J. Mach. Learn. Res., 13, 281–305, 2012.

Blanchard-Wrigglesworth, E., Webster, M. A., Farrell, S. L., and Bitz, C. M.: Reconstruction of snow on Arctic sea ice, J. Geophys. Res. Ocean., 123, 3588–3602, https://doi.org/10.1002/2017JC013364, 2018.

Boisvert, L. N., Webster, M. A., Petty, A. A., Markus, T., Cullather, R. I., and Bromwich, D. H.: Intercomparison of precipitation estimates over the Southern Ocean from atmospheric reanalyses, J. Clim., 33, 10627–10651, https://doi.org/10.1175/JCLI-D-20-0044.1, 2020.

Box, J. E., Bromwich, D. H., and Bai, L.-S.: Greenland ice sheet surface mass balance 1991–2000: Application of Polar MM5 mesoscale model and in situ data, J. Geophys. Res., 109, D16105, https://doi.org/10.1029/2003JD004451, 2004.

van den Broeke, M. R.: Spatial and temporal variation of sublimation on Antarctica: Results of a high-resolution general circulation model, J. Geophys. Res. Atmos., 102, 29765–29777, https://doi.org/10.1029/97JD01862, 1997.

Brucker, L. and Markus, T.: Arctic-scale assessment of satellite passive microwave-derived snow depth on sea ice using Operation IceBridge airborne data, J. Geophys. Res. Ocean., 118, 2892–2905, https://doi.org/10.1002/jgrc.20228, 2013.

Cabaj, A., Kushner, P. J., Fletcher, C. G., Howell, S., and Petty, A. A.: Constraining reanalysis snowfall over the Arctic Ocean using CloudSat observations, Geophys. Res. Lett., 47, e2019GL086426, https://doi.org/10.1029/2019GL086426, 2020.

Cabaj, A., Kushner, P. J., and Petty, A. A.: Automated calibration of a snow-on-sea-ice model, Earth Sp. Sci., 10, e2022EA002655, https://doi.org/10.1029/2022EA002655, 2023.

Campbell, E. C.: University of Washington Snow on Antarctic Ice Lagrangian (WASSAIL) model data, v1.0.0 (2003-2025), Zenodo [data set], https://doi.org/10.5281/zenodo.19507962, 2026a.

Campbell, E. C.: University of Washington Snow on Antarctic Ice Lagrangian (WASSAIL) model and analysis code, v1.0.0, Zenodo [code], https://doi.org/10.5281/zenodo.19509689, 2026b.

Campbell, E. C., Wilson, E. A., Moore, G. W. K., Riser, S. C., Brayton, C. E., Mazloff, M. R., and Talley, L. D.: Antarctic offshore polynyas linked to Southern Hemisphere climate anomalies, Nature, 570, 319–325, https://doi.org/10.1038/s41586-019-1294-0, 2019.

Cavalieri, D. J., Markus, T., and Comiso, J. C.: AMSR-E/Aqua Daily L3 12.5 km Brightness Temperature, Sea Ice Concentration, & Snow Depth Polar Grids (AE_SI12, version 3), NASA National Snow and Ice Data Center (NSIDC) Distributed Active Archive Center (DAAC) [data set], https://doi.org/10.5067/AMSR-E/AE_SI12.003, 2014.

Chung, Y.-C., Bélair, S., and Mailhot, J.: Blowing snow on Arctic sea ice: Results from an improved sea ice–snow–blowing snow coupled system, J. Hydrometeorol., 12, 678–689, https://doi.org/10.1175/2011JHM1293.1, 2011.

Clemens-Sewall, D., Polashenski, C., Frey, M. M., Cox, C. J., Granskog, M. A., Macfarlane, A. R., Fons, S. W., Schmale, J., Hutchings, J. K., von Albedyll, L., Arndt, S., Schneebeli, M., and Perovich, D.: Snow loss into leads in Arctic sea ice: Minimal in typical wintertime conditions, but high during a warm and windy snowfall event, Geophys. Res. Lett., 50, e2023GL102816, https://doi.org/10.1029/2023GL102816, 2023.

Copernicus Climate Change Service: ERA5 hourly data on single levels from 1940 to present, Copernicus Climate Change Service (C3S) Climate Data Store (CDS) [data set], https://doi.org/10.24381/cds.adbb2d47, 2023.

Déry, S. J. and Tremblay, L. B.: Modeling the effects of wind redistribution on the snow mass budget of polar sea ice, J. Phys. Oceanogr., 34, 258–271, https://doi.org/10.1175/1520-0485(2004)034<0258:MTEOWR>2.0.CO;2, 2004.

Déry, S. J. and Yau, M.-K.: Simulation of blowing snow in the Canadian Arctic using a double-moment model, Boundary-Layer Meteorol., 99, 297–316, https://doi.org/10.1023/A:1018965008049, 2001.

Déry, S. J. and Yau, M.-K.: Large-scale mass balance effects of blowing snow and surface sublimation, J. Geophys. Res. Atmos., 107, 4679, https://doi.org/10.1029/2001JD001251, 2002.

Dou, T., Xiao, C., Liu, J., Han, W., Du, Z., Mahoney, A. R., Jones, J., and Eicken, H.: A key factor initiating surface ablation of Arctic sea ice: earlier and increasing liquid precipitation, Cryosph., 13, 1233–1246, https://doi.org/10.5194/tc-13-1233-2019, 2019.

Dubey, U., Willmes, S., and Heinemann, G.: Southern Ocean sea-ice leads: first insights into regional lead patterns, seasonality, and trends, 2003–2023, Cryosph., 19, 3535–3552, https://doi.org/10.5194/tc-19-3535-2025, 2025.

Eicken, H., Lange, M. A., Hubberten, H.-W., and Wadhams, P.: Characteristics and distribution patterns of snow and meteoric ice in the Weddell Sea and their contribution to the mass balance of sea ice, Ann. Geophys., 12, 80–93, https://doi.org/10.1007/s00585-994-0080-x, 1994.

Eicken, H., Fischer, H., and Lemke, P.: Effects of the snow cover on Antarctic sea ice and potential modulation of its response to climate change, Ann. Glaciol., 21, 369–376, https://doi.org/10.1017/S0260305500016086, 1995.

Fichefet, T. and Morales Maqueda, M. A.: Modelling the influence of snow accumulation and snow-ice formation on the seasonal cycle of the Antarctic sea-ice cover, Clim. Dyn., 15, 251–268, https://doi.org/10.1007/s003820050280, 1999.

Fons, S., Kurtz, N., and Bagnardi, M.: A decade-plus of Antarctic sea ice thickness and volume estimates from CryoSat-2 using a physical model and waveform fitting, Cryosph., 17, 2487–2508, https://doi.org/10.5194/tc-17-2487-2023, 2023.

Franz, K. J., Hogue, T. S., and Sorooshian, S.: Operational snow modeling: Addressing the challenges of an energy balance model for National Weather Service forecasts, J. Hydrol., 360, 48–66, https://doi.org/10.1016/j.jhydrol.2008.07.013, 2008.

Fraser, A. D., Massom, R. A., Handcock, M. S., Reid, P., Ohshima, K. I., Raphael, M. N., Cartwright, J., Klekociuk, A. R., Wang, Z., and Porter-Smith, R.: Eighteen-year record of circum-Antarctic landfast-sea-ice distribution allows detailed baseline characterisation and reveals trends and variability, Cryosph., 15, 5061–5077, https://doi.org/10.5194/tc-15-5061-2021, 2021.

Garratt, J. R.: The atmospheric boundary layer, edited by: Houghton, J. T., Rycroft, M. J., and Dessler, A. J., Cambridge University Press, Cambridge, UK, 334 pp., ISBN 9780521380522, 1992.

Girotto, M., Formetta, G., Azimi, S., Bachand, C., Cowherd, M., De Lannoy, G., Lievens, H., Modanesi, S., Raleigh, M. S., Rigon, R., and Massari, C.: Identifying snowfall elevation patterns by assimilating satellite-based snow depth retrievals, Sci. Total Environ., 906, 167312, https://doi.org/10.1016/j.scitotenv.2023.167312, 2024.

Goosse, H. and Zunz, V.: Decadal trends in the Antarctic sea ice extent ultimately controlled by ice–ocean feedback, Cryosph., 8, 453–470, https://doi.org/10.5194/tc-8-453-2014, 2014.

Gordon, A. L., Chen, C.-T. A., and Metcalf, W. G.: Winter mixed layer entrainment of Weddell Deep Water, J. Geophys. Res., 89, 637–640, https://doi.org/10.1029/JC089iC01p00637, 1984.

Graham, R. M., Cohen, L., Ritzhaupt, N., Segger, B., Graversen, R. G., Rinke, A., Walden, V. P., Granskog, M. A., and Hudson, S. R.: Evaluation of six atmospheric reanalyses over Arctic sea ice from winter to early summer, J. Clim., 32, 4121–4143, https://doi.org/10.1175/JCLI-D-18-0643.1, 2019.

Groot Zwaaftink, C. D., Cagnati, A., Crepaz, A., Fierz, C., Macelloni, G., Valt, M., and Lehning, M.: Event-driven deposition of snow on the Antarctic Plateau: analyzing field measurements with SNOWPACK, Cryosph., 7, 333–347, https://doi.org/10.5194/tc-7-333-2013, 2013.

Haumann, F. A., Gruber, N., Münnich, M., Frenger, I., and Kern, S.: Sea-ice transport driving Southern Ocean salinity and its recent trends, Nature, 537, 89–92, https://doi.org/10.1038/nature19101, 2016.

Hersbach, H., Bell, B., Berrisford, P., Hirahara, S., Horányi, A., Muñoz-Sabater, J., Nicolas, J., Peubey, C., Radu, R., Schepers, D., Simmons, A., Soci, C., Abdalla, S., Abellan, X., Balsamo, G., Bechtold, P., Biavati, G., Bidlot, J., Bonavita, M., Chiara, G., Dahlgren, P., Dee, D., Diamantakis, M., Dragani, R., Flemming, J., Forbes, R., Fuentes, M., Geer, A., Haimberger, L., Healy, S., Hogan, R. J., Hólm, E., Janisková, M., Keeley, S., Laloyaux, P., Lopez, P., Lupu, C., Radnoti, G., Rosnay, P., Rozum, I., Vamborg, F., Villaume, S., and Thépaut, J.: The ERA5 global reanalysis, Q. J. R. Meteorol. Soc., 146, 1999–2049, https://doi.org/10.1002/qj.3803, 2020.

Holland, P. R. and Kimura, N.: Observed concentration budgets of Arctic and Antarctic sea ice, J. Clim., 29, 5241–5249, https://doi.org/10.1175/JCLI-D-16-0121.1, 2016.

Holland, P. R. and Kwok, R.: Wind-driven trends in Antarctic sea-ice drift, Nat. Geosci., 5, 872–875, https://doi.org/10.1038/ngeo1627, 2012.

Holland, P. R., Bruneau, N., Enright, C., Losch, M., Kurtz, N. T., and Kwok, R.: Modeled trends in Antarctic sea ice thickness, J. Clim., 27, 3784–3801, https://doi.org/10.1175/JCLI-D-13-00301.1, 2014.

Hunke, E. C., Lipscomb, W. H., Turner, A. K., Jeffery, N., and Elliott, S.: CICE: the Los Alamos sea ice model documentation and software user's manual (version 5.1, LA-CC-06-012), Los Alamos, NM, https://doi.org/10.5281/zenodo.19207490, 2015.

Ivanova, N., Pedersen, L. T., Tonboe, R. T., Kern, S., Heygster, G., Lavergne, T., Sørensen, A. M., Saldo, R., Dybkjær, G., Brucker, L., and Shokr, M.: Inter-comparison and evaluation of sea ice algorithms: Towards further identification of challenges and optimal approach using passive microwave observations, Cryosph., 9, 1797–1817, https://doi.org/10.5194/tc-9-1797-2015, 2015.

Jamieson, K. and Talwalkar, A.: Non-stochastic best arm identification and hyperparameter optimization, in: Proceedings of the 19th International Conference on Artificial Intelligence and Statistics, 240–248, 2016.

Jeffries, M. O., Krouse, H. R., Hurst-Cushing, B., and Maksym, T.: Snow-ice accretion and snow-cover depletion on Antarctic first-year sea-ice floes, Ann. Glaciol., 33, 51–60, https://doi.org/10.3189/172756401781818266, 2001.

Jordan, R. E., Andreas, E. L., and Makshtas, A. P.: Heat budget of snow-covered sea ice at North Pole 4, J. Geophys. Res. Ocean., 104, 7785–7806, https://doi.org/10.1029/1999JC900011, 1999.

Kacimi, S. and Kwok, R.: The Antarctic sea ice cover from ICESat-2 and CryoSat-2: freeboard, snow depth, and ice thickness, Cryosph., 14, 4453–4474, https://doi.org/10.5194/tc-14-4453-2020, 2020.

Karnin, Z., Koren, T., and Somekh, O.: Almost optimal exploration in multi-armed bandits, in: Proceedings of the 30th International Conference on Machine Learning, Atlanta, GA, 1238–1246, 2013.

Keenan, E., Wever, N., Dattler, M., Lenaerts, J. T. M., Medley, B., Kuipers Munneke, P., and Reijmer, C.: Physics-based SNOWPACK model improves representation of near-surface Antarctic snow and firn density, Cryosph., 15, 1065–1085, https://doi.org/10.5194/tc-15-1065-2021, 2021.

Kern, S., Ozsoy-Cicek, B., Willmes, S., Nicolaus, M., Haas, C., and Ackley, S.: An intercomparison between AMSR-E snow-depth and satellite C- and Ku-band radar backscatter data for Antarctic sea ice, Ann. Glaciol., 52, 279–290, https://doi.org/10.3189/172756411795931750, 2011.

King, J. C., Marshall, G. J., Colwell, S., Arndt, S., Allen-Sader, C., and Phillips, T.: The performance of the ERA-Interim and ERA5 atmospheric reanalyses over Weddell Sea pack ice, J. Geophys. Res. Ocean., 127, e2022JC018805, https://doi.org/10.1029/2022JC018805, 2022.

Kjellsson, J., Holland, P. R., Marshall, G. J., Mathiot, P., Aksenov, Y., Coward, A. C., Bacon, S., Megann, A. P., and Ridley, J.: Model sensitivity of the Weddell and Ross seas, Antarctica, to vertical mixing and freshwater forcing, Ocean Model., 94, 141–152, https://doi.org/10.1016/j.ocemod.2015.08.003, 2015.

Kojima, K.: Densification of seasonal snow cover, Phys. Snow Ice Proc., 1, 929–952, 1967.

Kong, F. and Yau, M.-K.: An explicit approach to microphysics in MC2, Atmosphere-Ocean, 35, 257–291, https://doi.org/10.1080/07055900.1997.9649594, 1997.

Kurtz, N. T. and Markus, T.: Satellite observations of Antarctic sea ice thickness and volume, J. Geophys. Res. Ocean., 117, C08025, https://doi.org/10.1029/2012JC008141, 2012.

Kwok, R. and Cunningham, G. F.: ICESat over Arctic sea ice: Estimation of snow depth and ice thickness, J. Geophys. Res., 113, C08010, https://doi.org/10.1029/2008JC004753, 2008.

Kwok, R. and Kacimi, S.: Three years of sea ice freeboard, snow depth, and ice thickness of the Weddell Sea from Operation IceBridge and CryoSat-2, Cryosph., 12, 2789–2801, https://doi.org/10.5194/tc-12-2789-2018, 2018.

Lago, V. and England, M. H.: Projected slowdown of Antarctic Bottom Water formation in response to amplified meltwater contributions, J. Clim., 32, 6319–6335, https://doi.org/10.1175/JCLI-D-18-0622.1, 2019.

Lawrence, I. R., Ridout, A. L., Shepherd, A., and Tilling, R.: A simulation of snow on Antarctic sea ice based on satellite data and climate reanalyses, J. Geophys. Res. Ocean., 129, e2022JC019002, https://doi.org/10.1029/2022JC019002, 2024.

Lecomte, O., Fichefet, T., Vancoppenolle, M., Domine, F., Massonnet, F., Mathiot, P., Morin, S., and Barriat, P.-Y.: On the formulation of snow thermal conductivity in large-scale sea ice models, J. Adv. Model. Earth Syst., 5, 542–557, https://doi.org/10.1002/jame.20039, 2013.

Lecomte, O., Fichefet, T., Flocco, D., Schroeder, D., and Vancoppenolle, M.: Interactions between wind-blown snow redistribution and melt ponds in a coupled ocean-sea ice model, Ocean Model., 87, 67–80, https://doi.org/10.1016/j.ocemod.2014.12.003, 2015.

Leonard, K. C. and Maksym, T.: The importance of wind-blown snow redistribution to snow accumulation on Bellingshausen Sea ice, Ann. Glaciol., 52, 271–278, https://doi.org/10.3189/172756411795931651, 2011.

Li, L. and Pomeroy, J. W.: Estimates of threshold wind speeds for snow transport using meteorological data, J. Appl. Meteorol., 36, 205–213, https://doi.org/10.1175/1520-0450(1997)036<0205:EOTWSF>2.0.CO;2, 1997.

Liston, G. E., Itkin, P., Stroeve, J., Tschudi, M., Stewart, J. S., Pedersen, S. H., Reinking, A. K., and Elder, K.: A Lagrangian snow-evolution system for sea-ice applications (SnowModel-LG): Part I—Model description, J. Geophys. Res. Ocean., 125, e2019JC015913, https://doi.org/10.1029/2019JC015913, 2020.

Lytle, V. I. and Ackley, S. F.: Snow-ice growth: A fresh-water flux inhibiting deep convection in the Weddell Sea, Antarctica, Ann. Glaciol., 33, 45–50, https://doi.org/10.3189/172756401781818752, 2001.

Maksym, T. and Markus, T.: Antarctic sea ice thickness and snow-to-ice conversion from atmospheric reanalysis and passive microwave snow depth, J. Geophys. Res. Ocean., 113, 1–18, https://doi.org/10.1029/2006JC004085, 2008.

Maksym, T., Stammerjohn, S. E., Ackley, S. F., and Massom, R.: Antarctic sea ice—A polar opposite?, Oceanography, 25, 140–151, https://doi.org/10.5670/oceanog.2012.88, 2012.

Markus, T. and Cavalieri, D. J.: Snow depth distribution over sea ice in the Southern Ocean from satellite passive microwave data, in: Antarctic sea ice: Physical processes, interactions and variability, vol. 74, American Geophysical Union, 19–39, https://doi.org/10.1029/AR074p0019, 1998.

Markus, T. and Cavalieri, D. J.: Interannual and regional variability of Southern Ocean snow on sea ice, Ann. Glaciol., 44, 53–57, https://doi.org/10.3189/172756406781811475, 2006.

Markus, T., Massom, R., Worby, A., Lytle, V., Kurtz, N., and Maksym, T.: Freeboard, snow depth and sea-ice roughness in East Antarctica from in situ and multiple satellite data, Ann. Glaciol., 52, 242–248, https://doi.org/10.3189/172756411795931570, 2011.

Martinson, D. G. and Iannuzzi, R. A.: Antarctic ocean-ice interaction: Implications from ocean bulk property distributions in the Weddell gyre, in: Antarctic Sea Ice: Physical Processes, Interactions and Variability (Antarctic Research Series), vol. 74, American Geophysical Union, Washington, D.C., 243–271, https://doi.org/10.1029/AR074p0243, 1998.

Massom, R. A., Drinkwater, M. R., and Haas, C.: Winter snow cover on sea ice in the Weddell Sea, J. Geophys. Res. Ocean., 102, 1101–1117, https://doi.org/10.1029/96JC02992, 1997.

Massom, R. A., Lytle, V. I., Worby, A. P., and Allison, I.: Winter snow cover variability on East Antarctic sea ice, J. Geophys. Res. Ocean., 103, 24837–24855, https://doi.org/10.1029/98JC01617, 1998.

Massom, R. A., Eicken, H., Hass, C., Jeffries, M. O., Drinkwater, M. R., Sturm, M., Worby, A. P., Wu, X., Lytle, V. I., Ushio, S., Morris, K., Reid, P. A., Warren, S. G., and Allison, I.: Snow on Antarctic sea ice, Rev. Geophys., 39, 413–445, https://doi.org/10.1029/2000RG000085, 2001.

Mazloff, M. R., Heimbach, P., and Wunsch, C.: An eddy-permitting Southern Ocean state estimate, J. Phys. Oceanogr., 40, 880–899, https://doi.org/10.1175/2009JPO4236.1, 2010.

Meier, W. N., Markus, T., and Comiso, J. C.: AMSR-E/AMSR2 Unified L3 Daily 12.5 km Brightness Temperatures, Sea Ice Concentration, Motion & Snow Depth Polar Grids (AU_SI12, version 1), NASA National Snow and Ice Data Center (NSIDC) Distributed Active Archive Center (DAAC) [data set], https://doi.org/10.5067/RA1MIJOYPK3P, 2018.

Meier, W. N., Fetterer, F., Windnagel, A. K., Stewart, J. S., and Stafford, T.: Near-Real-Time NOAA/NSIDC Climate Data Record of Passive Microwave Sea Ice Concentration (G10016, version 3), National Snow and Ice Data Center (NSIDC) [data set], https://doi.org/10.7265/j0z0-4h87, 2024a.

Meier, W. N., Fetterer, F., Windnagel, A. K., Stewart, J. S., and Stafford, T.: NOAA/NSIDC Climate Data Record of Passive Microwave Sea Ice Concentration (G02202, version 5), National Snow and Ice Data Center (NSIDC) [data set], https://doi.org/10.7265/rjzb-pf78, 2024b.

Merkouriadi, I., Cheng, B., Graham, R. M., Rösel, A., and Granskog, M. A.: Critical role of snow on sea ice growth in the Atlantic sector of the Arctic Ocean, Geophys. Res. Lett., 44, 10479–10485, https://doi.org/10.1002/2017GL075494, 2017.

Nakayama, Y., Malyarenko, A., Zhang, H., Wang, O., Auger, M., Nie, Y., Fenty, I., Mazloff, M., Köhl, A., and Menemenlis, D.: Evaluation of MITgcm-based ocean reanalyses for the Southern Ocean, Geosci. Model Dev., 17, 8613–8638, https://doi.org/10.5194/gmd-17-8613-2024, 2024.

Nicolaus, M., Haas, C., and Bareiss, J.: Observations of superimposed ice formation at melt-onset on fast ice on Kongsfjorden, Svalbard, Phys. Chem. Earth, Parts A/B/C, 28, 1241–1248, https://doi.org/10.1016/j.pce.2003.08.048, 2003.

Nicolaus, M., Hoppmann, M., Arndt, S., Hendricks, S., Katlein, C., König-Langlo, G., Nicolaus, A., Rossmann, L., Schiller, M., Schwegmann, S., Langevin, D., and Bartsch, A.: Snow height and air temperature on sea ice from Snow Buoy measurements, Alfred Wegener Institute, Helmholtz Center for Polar and Marine Research [data set], https://doi.org/10.1594/PANGAEA.875638, 2017.

Nicolaus, M., Hoppmann, M., Arndt, S., Hendricks, S., Katlein, C., Nicolaus, A., Rossmann, L., Schiller, M., and Schwegmann, S.: Snow depth and air temperature seasonality on sea ice derived from snow buoy measurements, Front. Mar. Sci., 8, 655446, https://doi.org/10.3389/fmars.2021.655446, 2021.

Pellichero, V., Sallée, J.-B., Chapman, C. C., and Downes, S. M.: The Southern Ocean meridional overturning in the sea-ice sector is driven by freshwater fluxes, Nat. Commun., 9, 1789, https://doi.org/10.1038/s41467-018-04101-2, 2018.

Petty, A. A., Webster, M., Boisvert, L., and Markus, T.: The NASA Eulerian Snow on Sea Ice Model (NESOSIM) v1.0: initial model development and analysis, Geosci. Model Dev., 11, 4577–4602, https://doi.org/10.5194/gmd-11-4577-2018, 2018.

Petty, A. A., Bagnardi, M., Kurtz, N. T., Tilling, R., Fons, S., Armitage, T., Horvat, C., and Kwok, R.: Assessment of ICESat-2 sea ice surface classification with Sentinel-2 imagery: implications for freeboard and new estimates of lead and floe geometry, Earth Sp. Sci., 8, e2020EA001491, https://doi.org/10.1029/2020EA001491, 2021.

Pitman, A. J., Yang, Z.-L., Cogley, J. G., and Henderson-Sellers, A.: Description of bare essentials of surface transfer for the Bureau of Meteorology Research Centre AGCM, Australia Bureau of Meteorology, 1991.

Purich, A. and Doddridge, E. W.: Record low Antarctic sea ice coverage indicates a new sea ice state, Commun. Earth Environ., 4, 314, https://doi.org/10.1038/s43247-023-00961-9, 2023.

Ranjithkumar, A., Duncan, E., Yang, X., Partridge, D. G., Lachlan-Cope, T., Gong, X., Nishimura, K., and Frey, M. M.: Direct observation of Arctic Sea salt aerosol production from blowing snow and modeling over a changing sea ice environment, Elem. Sci. Anthr., 13, 1–27, https://doi.org/10.1525/elementa.2024.00006, 2025.

Ricker, R., Hendricks, S., Helm, V., Skourup, H., and Davidson, M.: Sensitivity of CryoSat-2 Arctic sea-ice freeboard and thickness on radar-waveform interpretation, Cryosph., 8, 1607–1622, https://doi.org/10.5194/tc-8-1607-2014, 2014.

Roberts, A. F., Hunke, E. C., Kamal, S. M., Lipscomb, W. H., Horvat, C., and Maslowski, W.: A variational method for sea ice ridging in Earth system models, J. Adv. Model. Earth Syst., 11, 771–805, https://doi.org/10.1029/2018MS001395, 2019.

Rogers, R. R. and Yau, M.-K.: A short course in cloud physics, 3rd ed., Butterworth-Heinemann, Burlington, MA, 304 pp., ISBN 9780080570945, 1989.

Rostosky, P., Spreen, G., Gerland, S., Huntemann, M., and Mech, M.: Modeling the microwave emission of snow on Arctic sea ice for estimating the uncertainty of satellite retrievals, J. Geophys. Res. Ocean., 125, e2019JC015465, https://doi.org/10.1029/2019JC015465, 2020.

Schwegmann, S., Haas, C., Fowler, C., and Gerdes, R.: A comparison of satellite-derived sea-ice motion with drifting-buoy data in the Weddell Sea, Antarctica, Ann. Glaciol., 52, 103–110, https://doi.org/10.3189/172756411795931813, 2011.

Semtner, A. J.: A model for the thermodynamic growth of sea ice in numerical investigations of climate, J. Phys. Oceanogr., 6, 379–389, https://doi.org/10.1175/1520-0485(1976)006<0379:AMFTTG>2.0.CO;2, 1976.

Shen, X., Ke, C.-Q., and Li, H.: Snow depth product over Antarctic sea ice from 2002 to 2020 using multisource passive microwave radiometers, Earth Syst. Sci. Data, 14, 619–636, https://doi.org/10.5194/essd-14-619-2022, 2022.

Singh, H. K. A., Landrum, L., Holland, M. M., Bailey, D. A., and DuVivier, A. K.: An overview of Antarctic sea ice in the Community Earth System Model version 2, part I: Analysis of the seasonal cycle in the context of sea ice thermodynamics and coupled atmosphere-ocean-ice processes, J. Adv. Model. Earth Syst., 13, e2020MS002143, https://doi.org/10.1029/2020MS002143, 2021.

Slater, A. G., Pitman, A. J., and Desborough, C. E.: The validation of a snow parameterization designed for use in general circulation models, Int. J. Climatol., 18, 595–617, https://doi.org/10.1002/(SICI)1097-0088(199805)18:6<595::AID-JOC275>3.0.CO;2-O, 1998.

Song, Y., Behrangi, A., and Blanchard-Wrigglesworth, E.: Assessment of satellite and reanalysis cold season snowfall estimates over Arctic sea ice, Geophys. Res. Lett., 47, e2020GL088970, https://doi.org/10.1029/2020GL088970, 2020.

Spreen, G., Kaleschke, L., and Heygster, G.: Sea ice remote sensing using AMSR-E 89-GHz channels, J. Geophys. Res. Ocean., 113, C02S03, https://doi.org/10.1029/2005JC003384, 2008.

Stroeve, J., Nandan, V., Willatt, R., Dadic, R., Rostosky, P., Gallagher, M., Mallett, R., Barrett, A., Hendricks, S., Tonboe, R., McCrystall, M., Serreze, M., Thielke, L., Spreen, G., Newman, T., Yackel, J., Ricker, R., Tsamados, M., Macfarlane, A., Hannula, H.-R., and Schneebeli, M.: Rain on snow (ROS) understudied in sea ice remote sensing: a multi-sensor analysis of ROS during MOSAiC (Multidisciplinary drifting Observatory for the Study of Arctic Climate), Cryosph., 16, 4223–4250, https://doi.org/10.5194/tc-16-4223-2022, 2022.

Stull, R. B.: Meteorology for scientists and engineers, 2nd ed., Brooks/Cole, Belmont, CA, 502 pp., ISBN 9780534372149, 2000.

Sturm, M., Morris, K., and Massom, R. A.: The winter snow cover of the West Antarctic pack ice: Its spatial and temporal variability, in: Antarctic sea ice: Physical processes, interactions and variability, vol. 74, American Geophysical Union, 1–18, https://doi.org/10.1029/AR074p0001, 1998.

Sturm, M., Holmgren, J., and Perovich, D. K.: Winter snow cover on the sea ice of the Arctic Ocean at the Surface Heat Budget of the Arctic Ocean (SHEBA): Temporal evolution and spatial variability, J. Geophys. Res. Ocean., 107, 8047, https://doi.org/10.1029/2000JC000400, 2002.

Szanyi, S., Lukovich, J. V., Barber, D. G., and Haller, G.: Persistent artifacts in the NSIDC ice motion data set and their implications for analysis, Geophys. Res. Lett., 43, 10800–10807, https://doi.org/10.1002/2016GL069799, 2016.

Talley, L. D.: Freshwater transport estimates and the global overturning circulation: Shallow, deep and throughflow components, Prog. Oceanogr., 78, 257–303, https://doi.org/10.1016/j.pocean.2008.05.001, 2008.

Tilling, R. L., Ridout, A., Shepherd, A., and Wingham, D. J.: Increased Arctic sea ice volume after anomalously low melting in 2013, Nat. Geosci., 8, 643–646, https://doi.org/10.1038/ngeo2489, 2015.

Toyota, T., Massom, R., Lecomte, O., Nomura, D., Heil, P., Tamura, T., and Fraser, A. D.: On the extraordinary snow on the sea ice off East Antarctica in late winter, 2012, Deep Sea Res. Part II Top. Stud. Oceanogr., 131, 53–67, https://doi.org/10.1016/j.dsr2.2016.02.003, 2016.

Tschudi, M. A., Meier, W. N., Stewart, J. S., Fowler, C., and Maslanik, J.: Polar Pathfinder Daily 25 km EASE-Grid Sea Ice Motion Vectors (NSIDC-0116, version 4), NASA National Snow and Ice Data Center (NSIDC) Distributed Active Archive Center (DAAC) [data set], https://doi.org/10.5067/INAWUWO7QH7B, 2019a.

Tschudi, M. A., Meier, W. N., and Stewart, J. S.: Quicklook Arctic Weekly EASE-Grid Sea Ice Motion Vectors (NSIDC-0748, version 1), NASA National Snow and Ice Data Center (NSIDC) Distributed Active Archive Center (DAAC) [data set], https://doi.org/10.5067/O0XI8PPYEZJ6, 2019b.

Tschudi, M. A., Meier, W. N., and Stewart, J. S.: An enhancement to sea ice motion and age products at the National Snow and Ice Data Center (NSIDC), Cryosph., 14, 1519–1536, https://doi.org/10.5194/tc-14-1519-2020, 2020.

Virtanen, P., Gommers, R., Oliphant, T. E., Haberland, M., Reddy, T., Cournapeau, D., Burovski, E., Peterson, P., Weckesser, W., Bright, J., van der Walt, S. J., Brett, M., Wilson, J., Millman, K. J., Mayorov, N., Nelson, A. R. J., Jones, E., Kern, R., Larson, E., Carey, C. J., Polat, İ., Feng, Y., Moore, E. W., VanderPlas, J., Laxalde, D., Perktold, J., Cimrman, R., Henriksen, I., Quintero, E. A., Harris, C. R., Archibald, A. M., Ribeiro, A. H., Pedregosa, F., van Mulbregt, P., Vijaykumar, A., Bardelli, A. Pietro, Rothberg, A., Hilboll, A., Kloeckner, A., Scopatz, A., Lee, A., Rokem, A., Woods, C. N., Fulton, C., Masson, C., Häggström, C., Fitzgerald, C., Nicholson, D. A., Hagen, D. R., Pasechnik, D. V., Olivetti, E., Martin, E., Wieser, E., Silva, F., Lenders, F., Wilhelm, F., Young, G., Price, G. A., Ingold, G.-L., Allen, G. E., Lee, G. R., Audren, H., Probst, I., Dietrich, J. P., Silterra, J., Webber, J. T., Slavič, J., Nothman, J., Buchner, J., Kulick, J., Schönberger, J. L., de Miranda Cardoso, J. V., Reimer, J., Harrington, J., Rodríguez, J. L. C., Nunez-Iglesias, J., Kuczynski, J., Tritz, K., Thoma, M., Newville, M., Kümmerer, M., Bolingbroke, M., Tartre, M., Pak, M., Smith, N. J., Nowaczyk, N., Shebanov, N., Pavlyk, O., Brodtkorb, P. A., Lee, P., McGibbon, R. T., Feldbauer, R., Lewis, S., Tygier, S., Sievert, S., Vigna, S., Peterson, S., More, S., Pudlik, T., et al.: SciPy 1.0: fundamental algorithms for scientific computing in Python, Nat. Methods, 17, 261–272, https://doi.org/10.1038/s41592-019-0686-2, 2020.

Walter, B., Weigel, H., Wahl, S., and Löwe, H.: Wind tunnel experiments to quantify the effect of aeolian snow transport on the surface snow microstructure, Cryosph., 18, 3633–3652, https://doi.org/10.5194/tc-18-3633-2024, 2024.

Wang, C., Graham, R. M., Wang, K., Gerland, S., and Granskog, M. A.: Comparison of ERA5 and ERA-Interim near-surface air temperature, snowfall and precipitation over Arctic sea ice: effects on sea ice thermodynamics and evolution, Cryosph., 13, 1661–1679, https://doi.org/10.5194/tc-13-1661-2019, 2019.

Wang, J., Massonnet, F., Goosse, H., Luo, H., Barthélemy, A., and Yang, Q.: Synergistic atmosphere-ocean-ice influences have driven the 2023 all-time Antarctic sea-ice record low, Commun. Earth Environ., 5, 415, https://doi.org/10.1038/s43247-024-01523-3, 2024a.

Wang, Z., Fraser, A. D., Reid, P., O'Farrell, S., and Coleman, R.: Antarctic sea ice surface temperature bias in atmospheric reanalyses induced by the combined effects of sea ice and clouds, Commun. Earth Environ., 5, 552, https://doi.org/10.1038/s43247-024-01692-1, 2024b.

Webster, M. A., Gerland, S., Holland, M., Hunke, E. C., Kwok, R., Lecomte, O., Massom, R. A., Perovich, D. K., and Sturm, M.: Snow in the changing sea-ice systems, Nat. Clim. Chang., 8, 946–953, https://doi.org/10.1038/s41558-018-0286-7, 2018.

Weiss, A. I., King, J., Lachlan-Cope, T., and Ladkin, R.: On the effective aerodynamic and scalar roughness length of Weddell Sea ice, J. Geophys. Res., 116, D19119, https://doi.org/10.1029/2011JD015949, 2011.

Wilson, E. A., Riser, S. C., Campbell, E. C., and Wong, A. P. S.: Winter upper-ocean stability and ice-ocean feedbacks in the sea ice-covered Southern Ocean, J. Phys. Oceanogr., 49, 1099–1117, https://doi.org/10.1175/JPO-D-18-0184.1, 2019.

Worby, A. P., Geiger, C. A., Paget, M. J., Van Woert, M. L., Ackley, S. F., and DeLiberty, T. L.: Thickness distribution of Antarctic sea ice, J. Geophys. Res., 113, C05S92, https://doi.org/10.1029/2007JC004254, 2008.

Yamazaki, T., Kondo, J., Sakuraoka, T., and Nakamura, T.: A one-dimensional model of the evolution of snow-cover characteristics, Ann. Glaciol., 18, 22–26, https://doi.org/10.1017/S0260305500011204, 1993.

Yan, Z., Wang, Y., Pang, X., and He, B.: An improved Antarctic sea-ice snow depth product from FY-3 MWRI with enhanced seasonal adaptability, Big Earth Data, in press, https://doi.org/10.1080/20964471.2026.2620844, 2026.

Yuan, X., Patoux, J., and Li, C.: Satellite-based midlatitude cyclone statistics over the Southern Ocean: 2. Tracks and surface fluxes, J. Geophys. Res., 114, D04106, https://doi.org/10.1029/2008JD010874, 2009.